

Protecting LHC IP1/IP5 Components Against Radiation Resulting from Colliding Beam Interactions*

N.V. Mokhov, I.L. Rakhno, J.S. Kerby, J.B. Strait

Fermilab, P.O. Box 500, Batavia, IL 60510, USA

April 9, 2003

Abstract

Beam-induced energy deposition in the LHC high luminosity interaction region (IR) components due to both pp collisions and beam loss in the IR vicinity is a significant challenge for the design of the high luminosity insertions. It was shown in our previous studies that a set of absorbers would reduce both the peak power density and total heat load to tolerable levels. In this paper the results of further optimization and comprehensive MARS calculations are summarized for the LHC lattice, version 6.4, for the updated IP1 and IP5 layouts and a baseline pp -collision source term. Power density, power dissipation, particle fluxes and spectra, accumulated dose and residual dose rates are studied in the components of the inner triplets including their TAS absorbers, the TAN neutral beam absorbers, separation dipoles, and quadrupoles of the outer triplets and possible collimators there. Results are given for the nominal luminosity of $10^{34} \text{ cm}^{-2} \text{ s}^{-1}$. The current design is proved to provide the best safety margin under realistic engineering constraints. Consideration is limited to luminosity-driven energy deposition effects in the inner and outer triplets. Impact of beam loss of circulating and misbehaved beams on the machine and detector components is considered elsewhere.

*Work supported by the Universities Research Association, Inc., under contract DE-AC02-76CH03000 with the U. S. Department of Energy.

Contents

1	Introduction	3
2	IP1 and IP5 Regions	3
2.1	Original configuration	3
2.2	MARS modeling	5
2.3	pp interaction rate	7
2.4	Design constraints	8
3	Front Absorber TAS	8
4	Inner Triplet	15
4.1	Earlier design	15
4.2	Slide bearings	19
4.3	DFBX feedboxes	19
4.4	Towards final design	20
5	TAN, D2 and Outer Triplet	33
5.1	Neutral particle absorber TAN	33
5.2	Radiation in TAN-D2 transition	40
5.3	Separation dipole and outer triplet	48
6	Uncertainties	53
7	Summary	53
8	Acknowledgments	53

1 Introduction

The Large Hadron Collider (LHC) [1] under construction at CERN, will produce pp collisions at center-of-mass energy $\sqrt{s}=14$ TeV and luminosity $L=10^{34}$ cm $^{-2}$ s $^{-1}$. The interaction rate of 8×10^8 s $^{-1}$ represents a power of almost 900 W per beam, the majority of which is directed towards the low- β insertions. Previous studies [2, 3, 4, 5, 6] have identified this as a serious problem and proposed the ways to mitigate it. The quadrupole fields sweep the secondary particles into the coils preferentially along the vertical and horizontal planes, giving rise to local peak power density ϵ_{max} as much as an order of magnitude larger than the average. Tests of porous cable insulation systems [7] and calculations concerning the insulation system to be used in the Fermilab-built LHC IR quadrupoles [8, 9] have shown that up to about 1.6 mW/g of heat can be removed while keeping the coil below the magnet quench temperature. Since our previous studies, which presented an optimized set of absorbers to protect the magnets, the optics design of the IRs has changed, better understanding of practical possibilities with quadrupole cooling and shielding has happened, and the MARS14 code [10] used for simulation of hadronic and electromagnetic cascades and induced energy deposition and radiation effects has undergone substantial improvements including implementation of the latest version of the DPMJET event generator [11] for pp collisions. Below summary results of extensive studies of the IP1 and IP5 high luminosity insertions are presented.

2 IP1 and IP5 Regions

2.1 Original configuration

The studies described in this paper are based on the versions 6.2 and 6.4 of the LHC optics [12]. The inner triplet consists of 70-mm coil aperture superconducting (SC) quadrupoles – 6.3-m long Q1 and Q3 (KEK) and 5.5-m long Q2a and Q2b (FNAL) – which are powered in series and operate at 199.46 T/m. Four corrector magnets – MCBX1, MCBX2, MQSXA and MCBXA of the same or larger coil apertures – provide tunability and the additional strength required. The design also includes the DFBX feedbox. A room temperature beam separation-recombination dipole D1 made of six 3.4-m long modules operates at 1.27 T, while a SC beam separation-recombination dipole D2 of 80-mm coil apertures separated by 188 mm operates at 2.74 T. The Q4 and Q5 quadrupoles of the outer triplet operate at 62.99 T/m and 95.15 T/m, respectively. The interaction plane is horizontal in IP5 and vertical in IP1 with a half crossing angle $\alpha=150$ μ rad.

To protect SC magnets against debris generated in the pp collisions and in the near beam elements, a set of absorbers was designed on the basis of energy deposition MARS calculations. It included the 1.8-m long 34-mm aperture TAS front absorber (former TAS1) at 19.45 m from the interaction point (IP), the inner absorber in the Q1 quadrupole, the TASA (between Q1 and Q2a) and TASB (between Q2b and Q3) intermediate absorbers, and the TAN neutral beam absorber in front of the D2 dipole. Their parameters were optimized over the years via the MARS runs to provide better protection and to meet practical requirements at the same time (see, e.g., Ref. [2, 5, 6]).

Fig. 1 shows the inner triplet configuration. The two curves show the approximate “ $n1 = 7$ ” beam envelope for injection and collision optics, including closed orbit and mechanical tolerances, according to the calculation in [13]. The collision optics case corresponds to $E=7$ TeV, $\beta^* = 0.5$ m, $\alpha=\pm 150$ μ rad, either vertical or horizontal crossing plane. The injection envelope corresponds to 450 GeV, $\beta^* = 18$ m, $\alpha=\pm 160$ μ rad, either crossing plane, with transverse beam separation at the IP being equal to 2.5 mm [14]. The aperture limitation occurs under low-beta conditions for collisions because of the wonders of a large β^* at injection. Fig. 2 shows the inner triplet implementation into the MARS model.

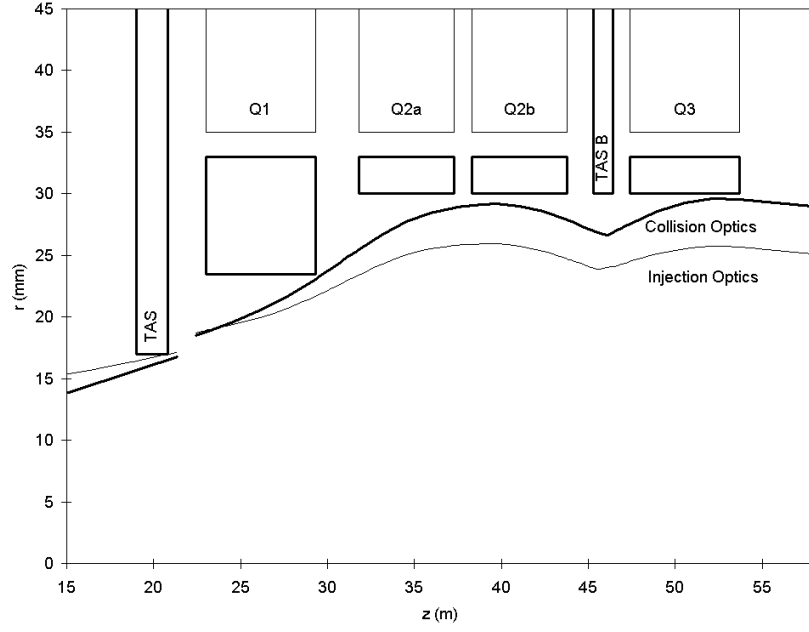


Figure 1: The LHC low- β insertions including absorbers: schematic view with the beam envelopes.

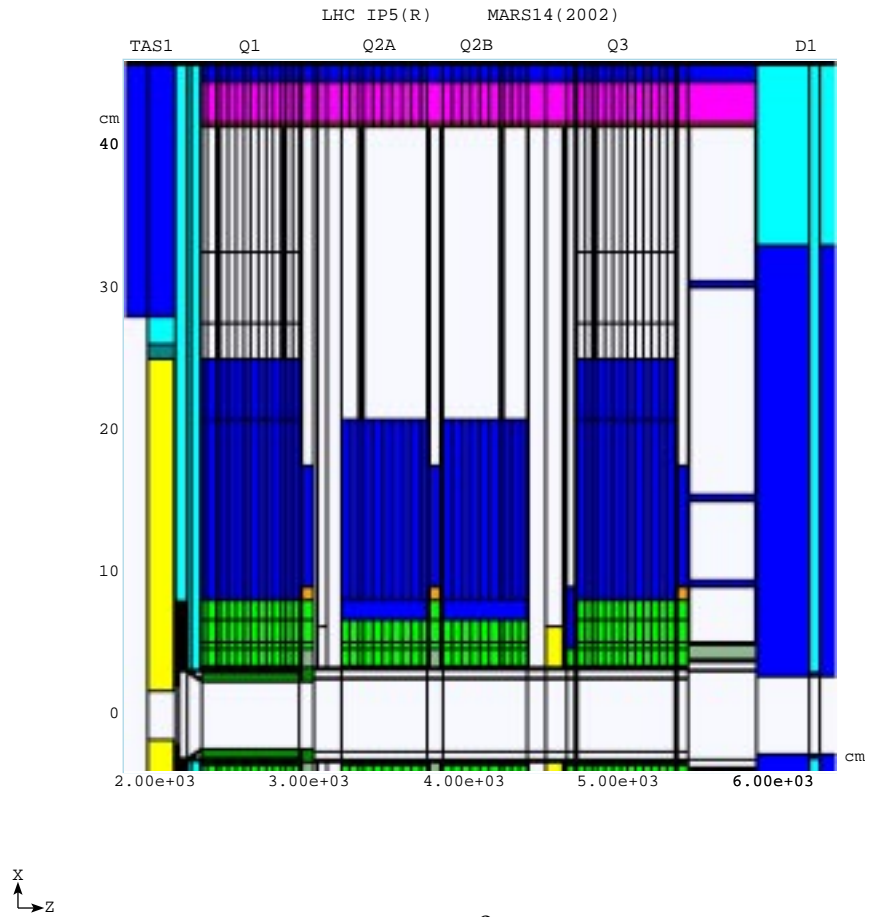


Figure 2: The LHC IP5 low- β insertion MARS model.

2.2 MARS modeling

All essential components situated in the tunnel of the IP1(R) and IP5(R) regions of 215-m long are implemented into the MARS14 model with a detailed description of their geometry, materials and magnetic field distributions. The model includes all the beam line, cryogenic and protection elements, tunnel, first meters of rock (molasse) outside the tunnel, as well as near beam components and solenoidal magnetic fields of the ATLAS and CMS detectors for the IP1 and IP5, respectively. Figs. 3 and 4 show the interaction region beam elements and their placement in the tunnel as modeled in the MARS14 code.

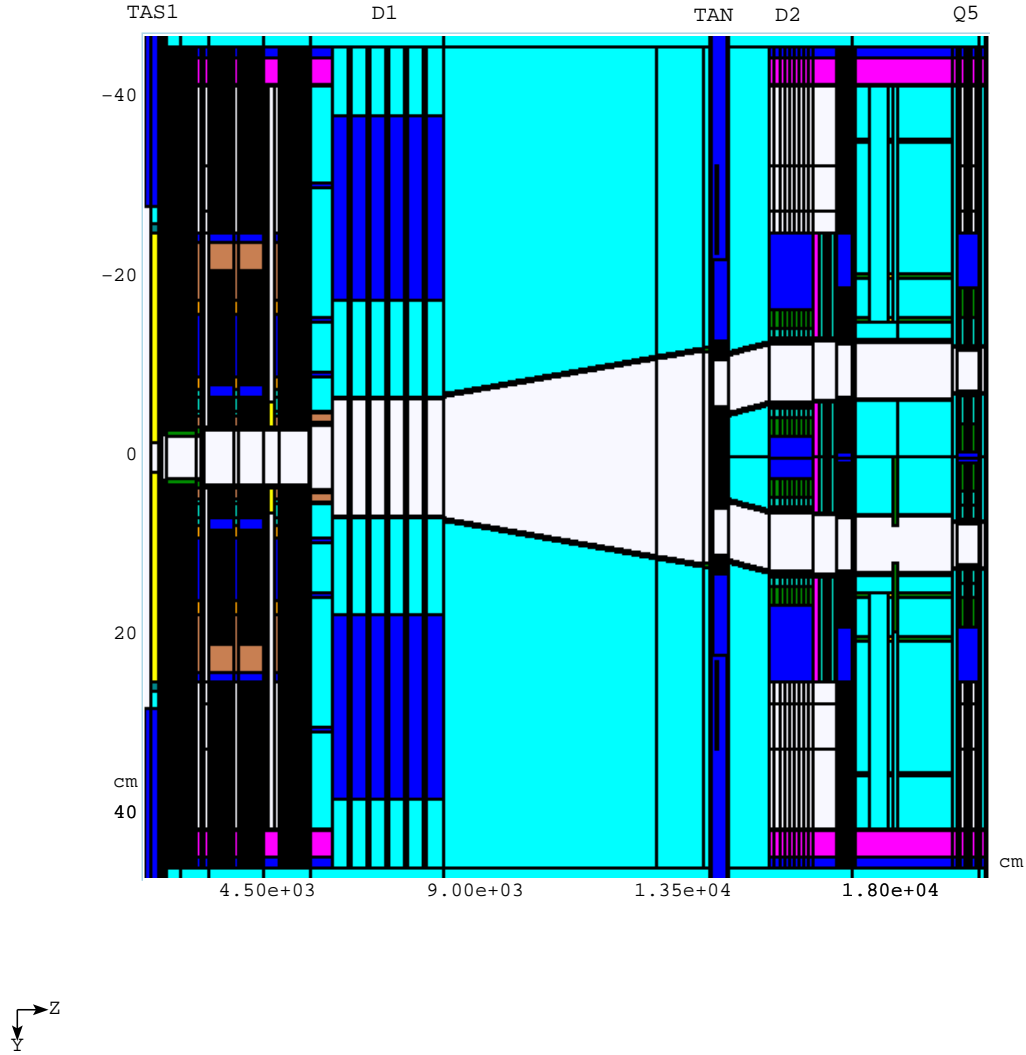


Figure 3: IP5 MARS model.

The two-dimensional fine grid magnetic field maps calculated with POISSON and OPERA for KEK and FNAL low- β quadrupoles, separation dipoles D1 and D2, and O4 and Q5 quadrupoles of the outer triplet are implemented to the MARS model (Fig. 5). There are four radial bins in the quadrupole coils, the first bin corresponds to the inner SC coil in Q1 and Q3, while the first coil of Q2a and Q2b is composed of the first and second radial bins.

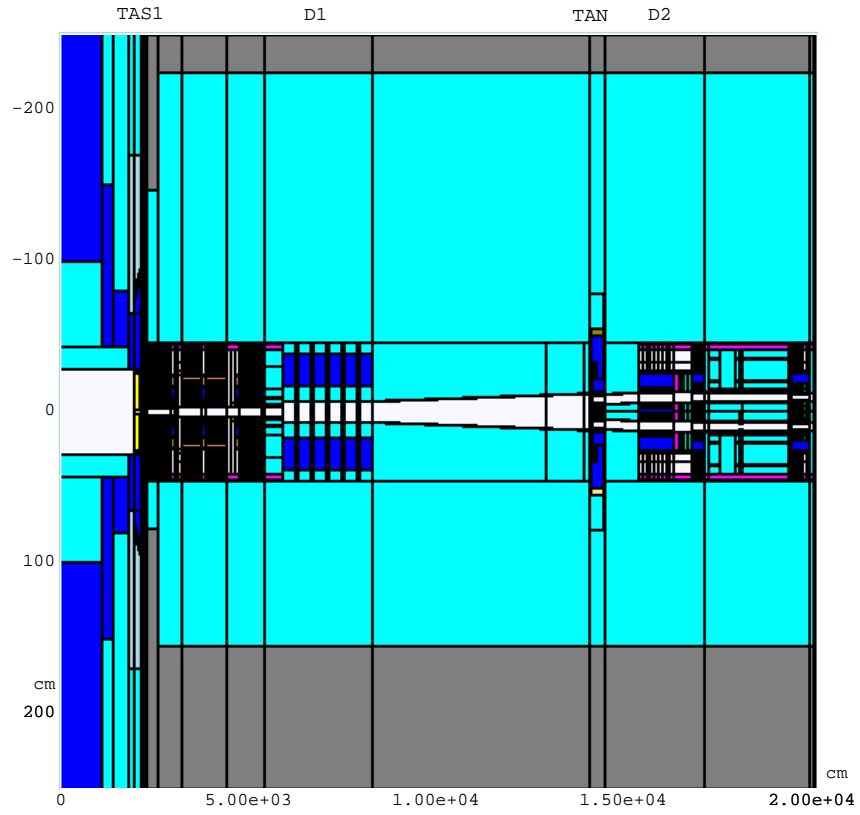


Figure 4: IP5 MARS model: overall plan view.

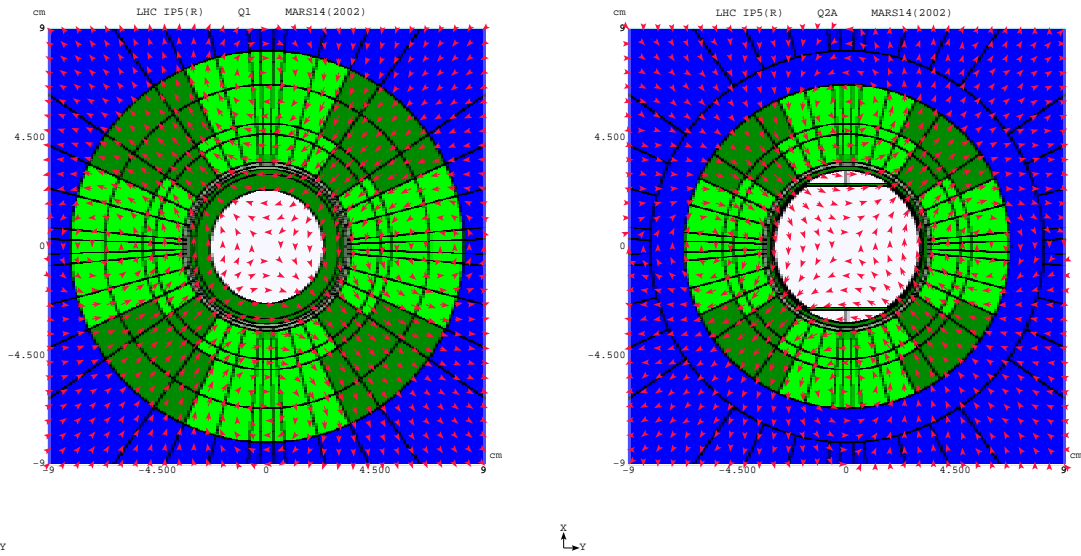


Figure 5: MARS models of the Q1 (left) and Q2a (right) quadrupoles.

Horizontal crossing is modeled in the IP5 with correspondingly oriented beam pipes, while it is modeled vertically in the IP1. Note that MARS uses the right-handed coordinate system, *i.e.*, x -axis is up, y -axis is to the right, and z -axis is along the beam away from the IP. The cut-off energy is 0.1 MeV for all particles except for neutrons which are followed down to thermal energies (~ 0.00215 eV). Calculated are 3-D distributions of particle flux Φ , energy deposition or power density ϵ , yearly accumulated dose D , power dissipation or dynamic heat load P , residual dose rate P_γ and various derivatives and integrals of these such as local peak power density ϵ_{max} , values related to operation and beam instrumentation etc. Results are given for the nominal luminosity of $10^{34} \text{ cm}^{-2}\text{s}^{-1}$. Consideration is limited to luminosity-driven energy deposition effects in the inner and outer triplets. Impact of the circulating and misbehaved beam on the machine and detector components is considered elsewhere [15, 16, 17].

2.3 pp interaction rate

To get an absolute normalization of the calculated results, one needs to know the pp non-elastic interaction rates at the IP1 and IP5: N_1 (s^{-1}) for power density and background-like values, N_2 (yr^{-1}) for yearly-accumulated effects, and N_3 (per 20 years) for the machine (detector) lifetime dose estimate. At the baseline luminosity $L=10^{34} \text{ cm}^{-2}\text{s}^{-1}$, $N_1=8 \times 10^8$ non-elastic (inelastic+diffractive) interactions per second, assuming 70 and 80 mb for inelastic and non-elastic cross-sections at $\sqrt{s}=14$ TeV, respectively. Then, with Ref. [18], one can conclude that

- The collider is expected to deliver protons for physics 180 days per year during its 20 years of operation.
- Yearly number of interactions at the IP1 and IP5, based on the averaged luminosity and a 24 hour average is $N_2=3.5 \times 10^8 \times 24(\text{hr}) \times 3600(\text{s/hr}) \times 180(\text{days}) = 6.22 \times 10^{15}$ non-elastic interactions per year or 5.44×10^{15} inelastic interactions per year.
- Luminosity profile assumes 1/10, 1/3 and 2/3 of the design luminosity for the first, second and third year and the design value of 10^{34} after that. This gives us 18.1 years of physics at the above rate over 20 years of operation.
- To calculate the machine (detector) lifetime dose, one should use $N_3 = 1.13 \times 10^{17}$ non-elastic or 0.98×10^{17} inelastic interactions per 20 years.

2.4 Design constraints

The protection system design constraints used in this study are as follows:

1. Baseline luminosity of $10^{34} \text{ cm}^{-2}\text{s}^{-1}$.
2. Keep *geometrical aperture larger than “ $n_l = 7$ ”* for injection and collision optics, including closed orbit and mechanical tolerances.
3. *Quench stability*: keep peak power density ϵ_{max} , which can be as much as an order of magnitude larger than the azimuthal average, below the quench limit with *a safety margin of a factor of 3*.
4. Use *1.6 mW/g as a quench limit*. For many years, the estimated quench limit for the LHC high-gradient quadrupoles was 1.2 mW/g. Tests of porous cable insulation systems and recent calculations concerning the insulation system to be used in the Fermilab-built LHC IR quadrupoles (MQXB) have shown that up to about 1.6 mW/g of heat can be removed while keeping the coil below the magnet quench temperature.
5. Rely on *radiation-hard materials*. With the above levels, the estimated lifetime will exceed then 7 years at the baseline luminosity even in the hottest spots.
6. Keep *dynamic heat loads below about 10 W/m*.
7. *Hands-on maintenance*: keep residual dose rates on the component outer surfaces below about 0.1 mSv/hr.
8. Always obey *engineering constraints*.

3 Front Absorber TAS

The TAS (former TAS1) absorbers in front of the first low- β quadrupoles are designed as a frontline system to protect the inner triplet by catching the particles originating from the IP and the cascades initiated by them. TAS’s parameters were optimized over years. Currently the TAS are at 19.45 m from the IP in the IP1 and IP5, made of copper, 1.8-m long and 1.7 cm inner and 25 cm outer radii. At design luminosity, they catch 184 W of collision power on each side of the IP. Figs. 6 and 7 show azimuthally averaged two-dimensional distributions of particle fluxes above 0.1 MeV in the TAS, interconnect region and upstream end of Q1. Two-dimensional isocontours of power density, accumulated dose, prompt dose equivalent and residual dose rate on contact (after 30-day irradiation and 1-day cooling) are presented in Figs. 8 and 9. The distributions are very similar for the IP1 and IP5. One clearly sees: rather uniform neutron flux distribution; the electromagnetic origin of energy deposition in first 30 cm of the TAS with a peak at 15 cm followed by a hadron-induced part; streaming of radiation through the air-gap at $26 < r < 28$ cm; very high levels of both instantaneous (prompt) dose and residual dose.

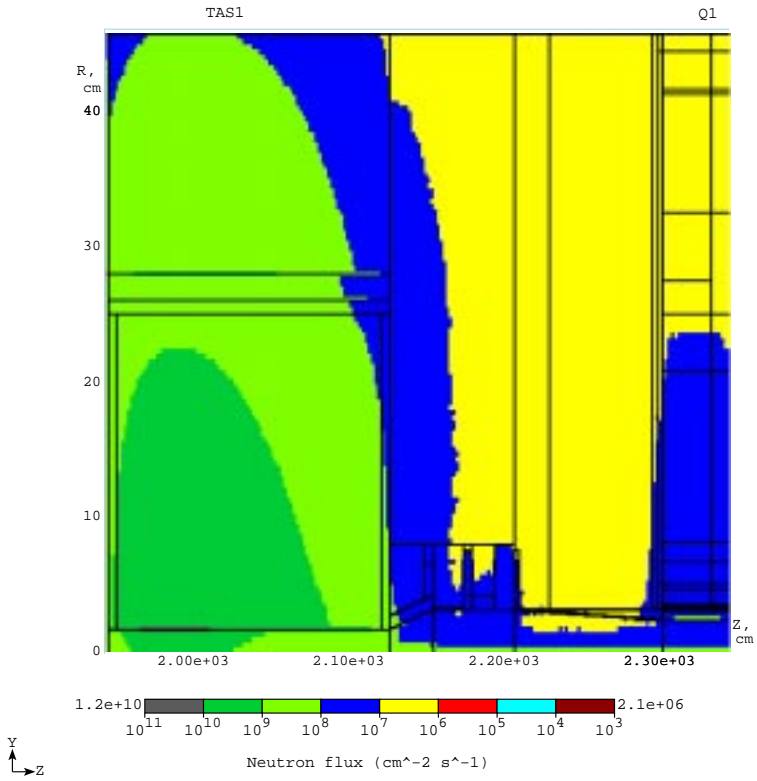
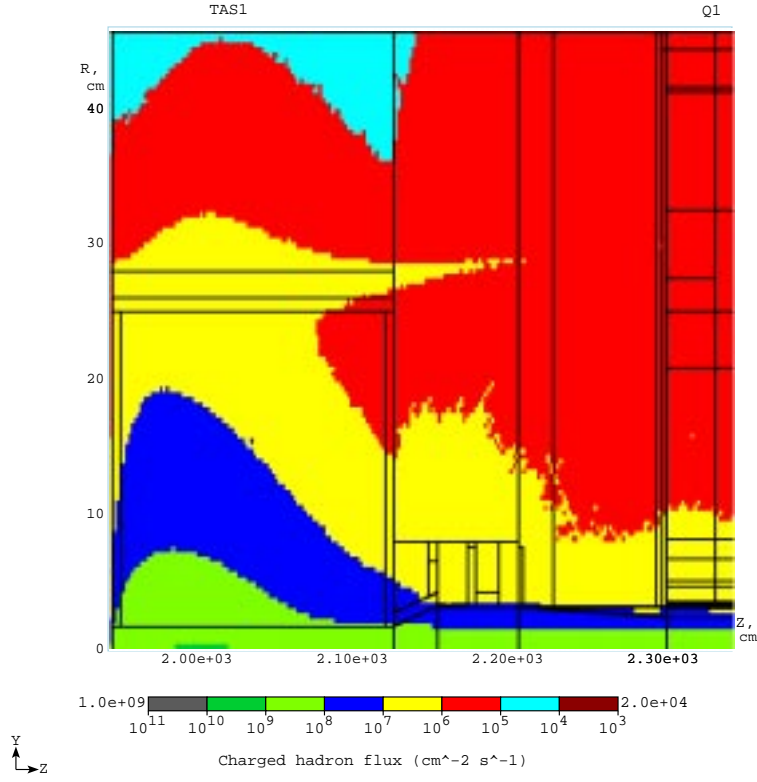


Figure 6: Azimuthally averaged charged hadron (top) and neutron (bottom) flux isocontours ($\text{cm}^{-2}\text{s}^{-1}$) in the TAS-Q1 region at the baseline luminosity. $E_{th}=0.1$ MeV.

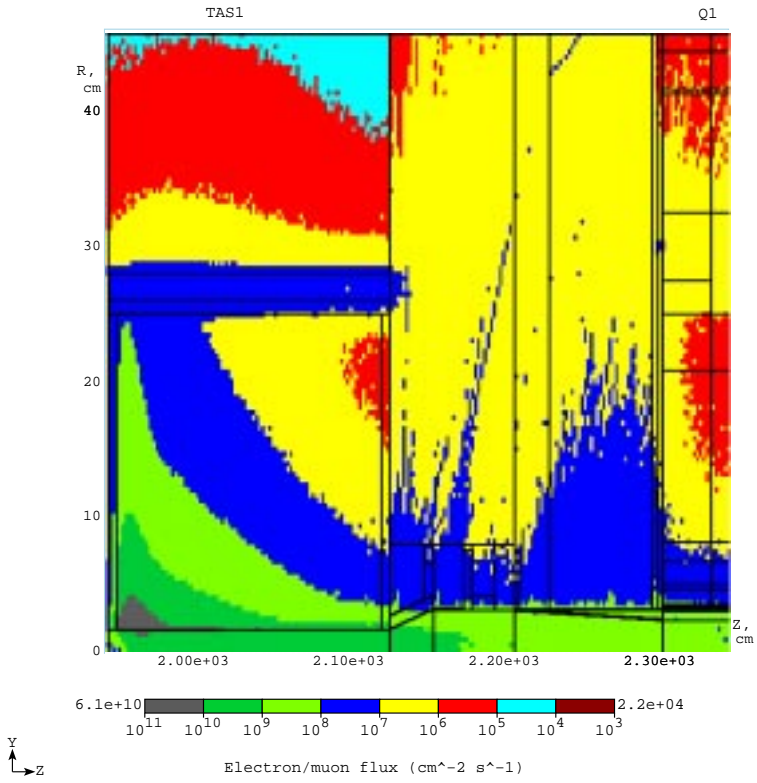
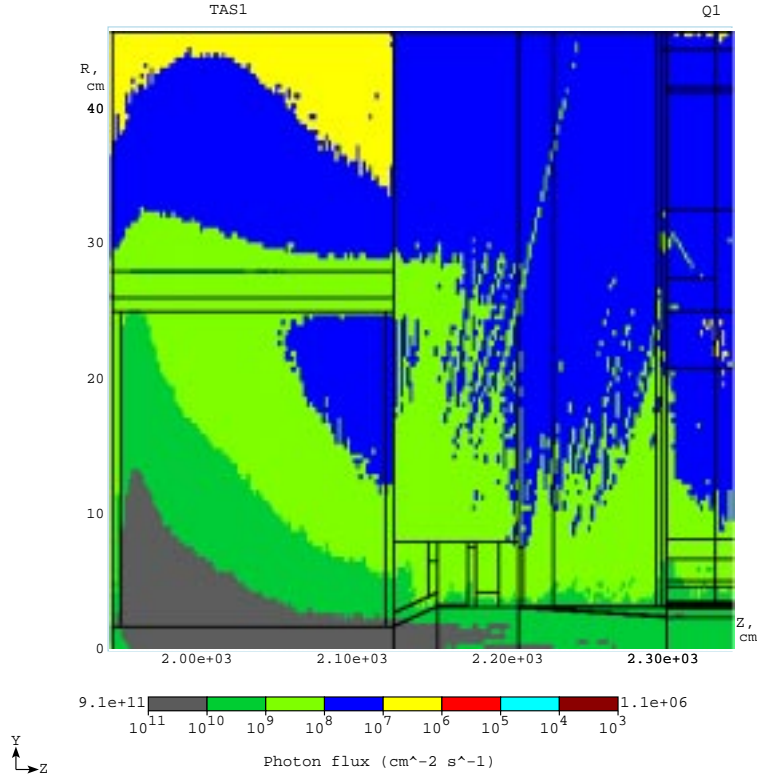


Figure 7: Azimuthally averaged photon (top) and $e^\pm + \mu^\pm$ (bottom) flux isocontours (cm⁻²s⁻¹) in the TAS-Q1 region at the baseline luminosity. $E_{th}=0.1$ MeV.

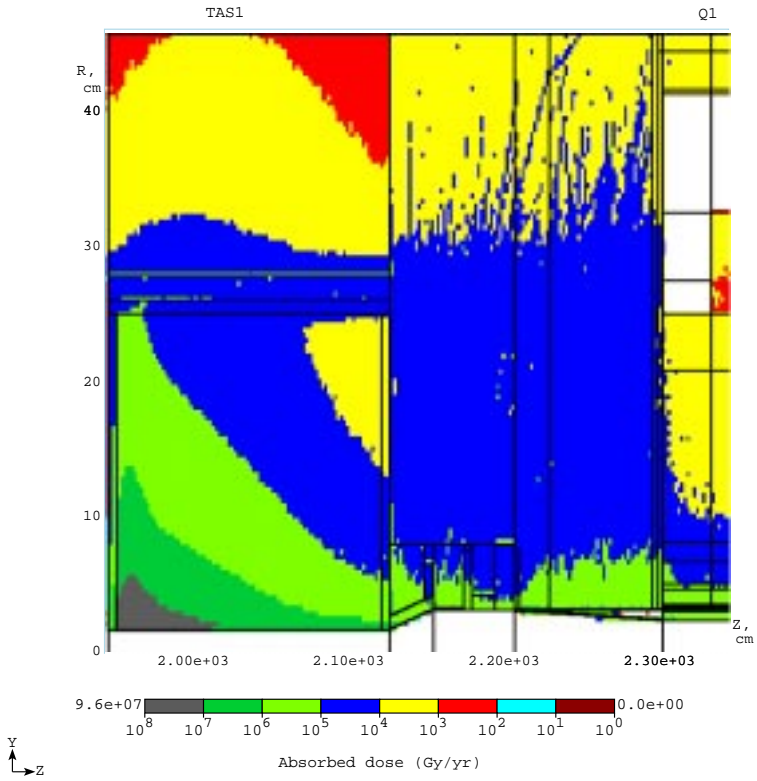
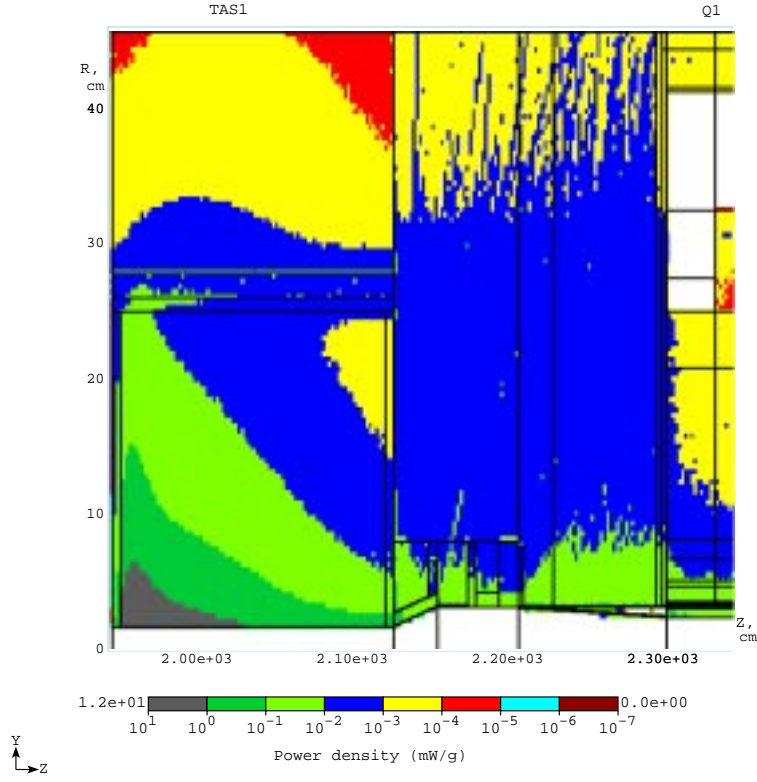


Figure 8: Azimuthally averaged power density in mW/g (top) and absorbed dose in Gy/yr (bottom) in the TAS-Q1 region at the baseline luminosity.

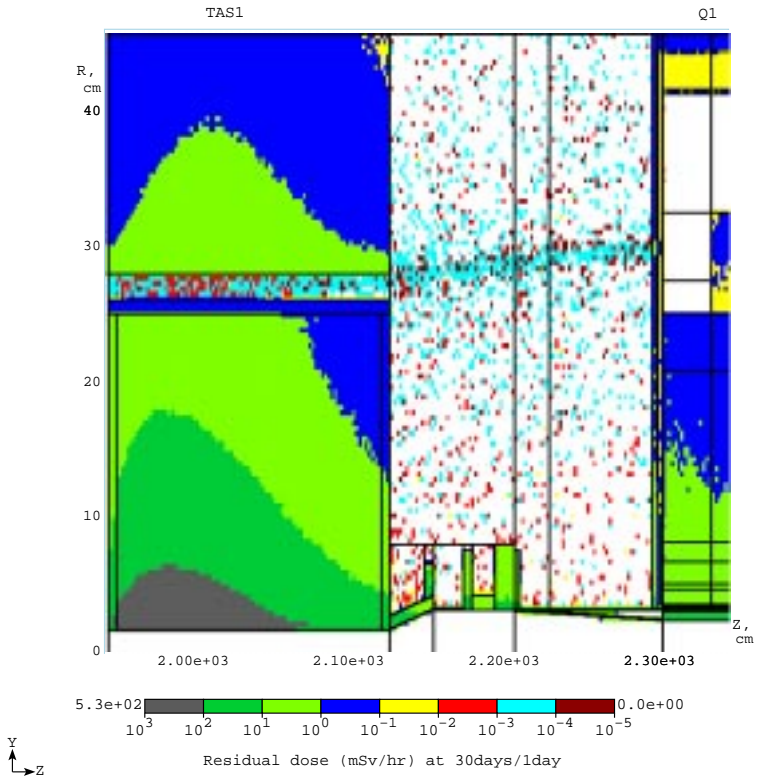
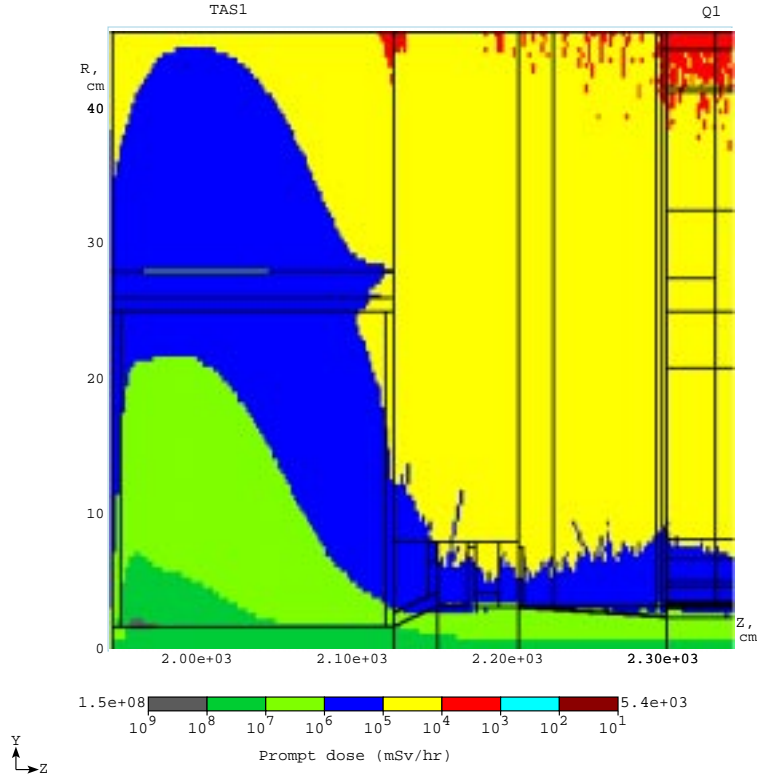


Figure 9: Azimuthally averaged prompt dose equivalent (top) and residual dose rate on contact after 30-day irradiation and 1-day cooling (bottom) in mSv/hr in the TAS-Q1 region at the baseline luminosity.

Particle fluxes ($E > 0.1$ MeV) at the longitudinal peak in the innermost layer of the IP1/IP5 TAS absorbers in $\text{cm}^{-2}\text{s}^{-1}$ are 1×10^{10} for neutrons, 8×10^8 for charged hadrons, 8×10^{11} for photons, 7×10^{10} for electrons and 1×10^6 for muons. Fig. 10 (left) gives longitudinal distribution of power density in three radial positions: close to the aperture, in the middle and close to the TAS outer radius. The maximum of 12.5 mW/g (or 100 MGy/yr) at 15 cm ($z=1960$ cm) is determined by photons and electrons coming to the absorber, while a slope after 35 cm is driven by cascades induced in the TAS body by incident hadrons. Radial distributions of power density at the TAS entrance (1 cm), cascade maximum (15 cm) and its back (179 cm) are presented in Fig. 10 (right). Note a significant contribution at large radius of radiation streaming through the air gap. Irradiation and cooling time dependencies of the residual dose rate on contact at the IP side and Q1 side of the TAS are shown in Fig. 11.

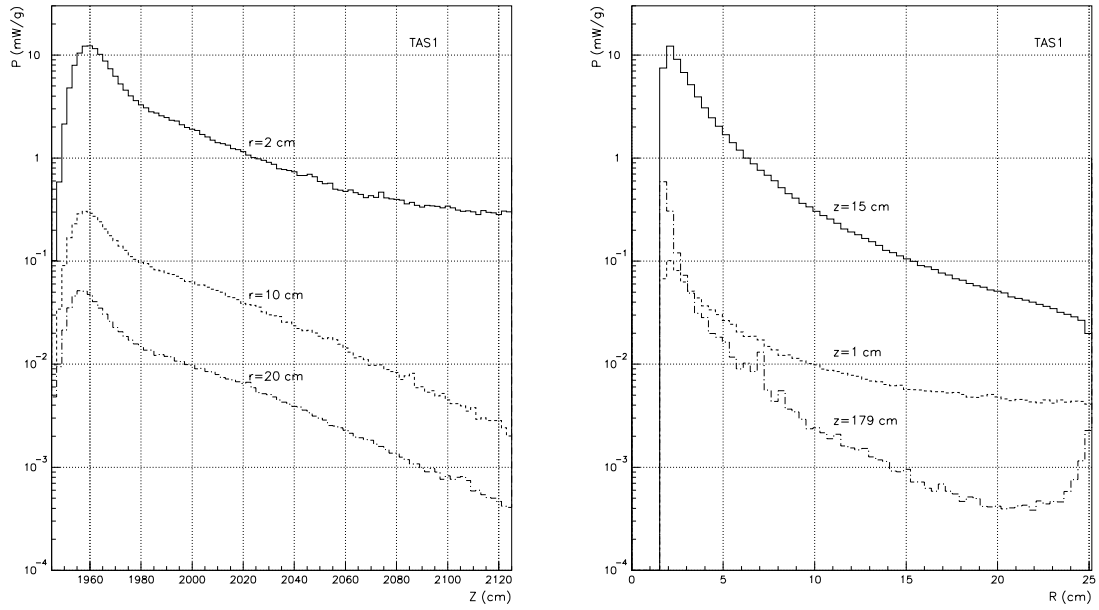


Figure 10: Longitudinal (left) and radial (right) distributions of power density (mW/g) at several locations in the TAS absorber.

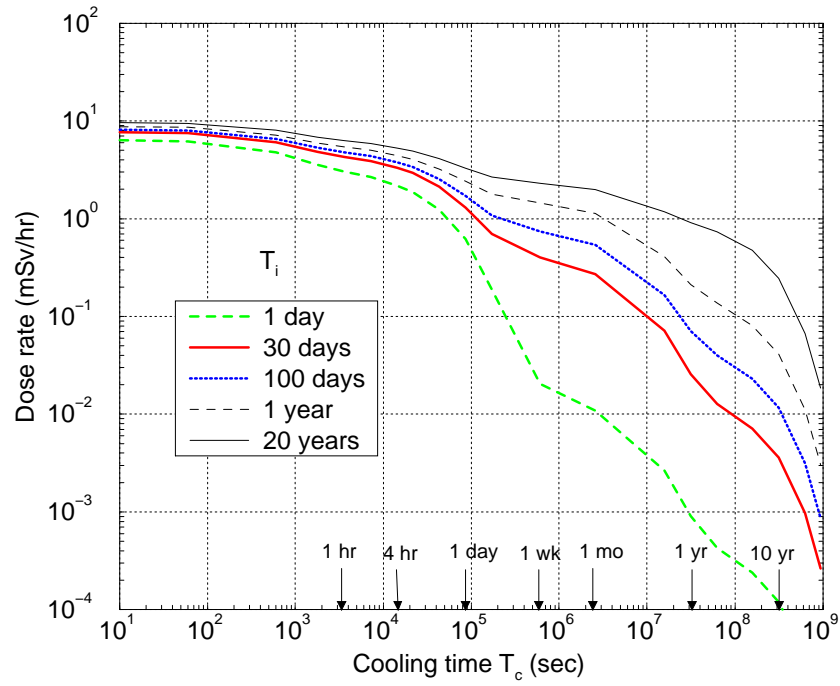
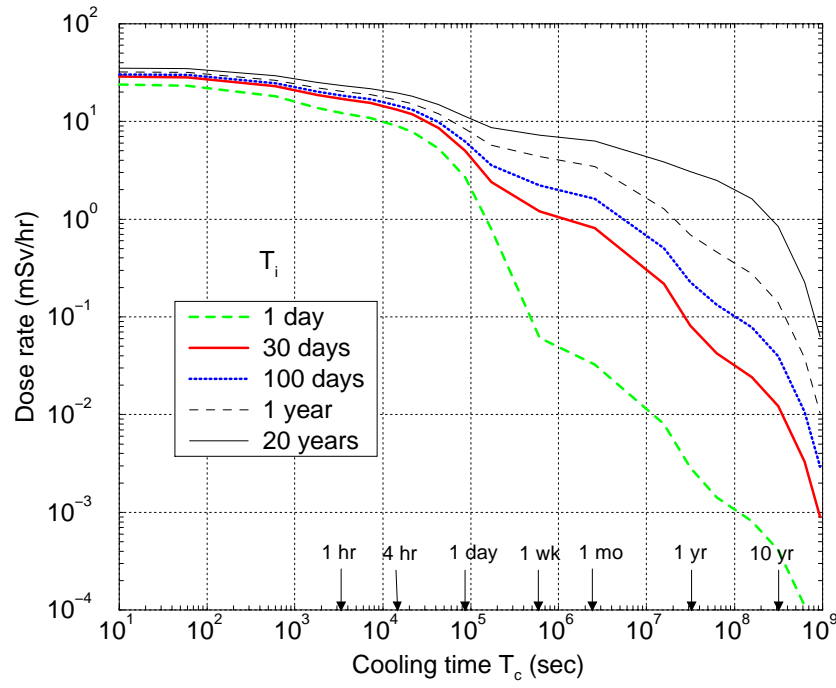


Figure 11: Averaged over surface residual dose rate (mSv/hr) on the IP side ($z=1945$ cm, top) and Q1 side ($z=2125$ cm, bottom) of the TAS vs irradiation and cooling times.

4 Inner Triplet

The structure of the inner triplet has been under investigation for several years. This section describes a preliminary design based on earlier MARS studies, some specific components proposed and optimized over years, and a final/current design proved to provide the best safety margin under more realistic engineering constraints.

4.1 Earlier design

The following protection system was designed as a result of our initial investigations: the TAS copper absorber, a stainless steel (SS) absorber ($23.5 < r < 33.3$ mm) inside the 35-mm radius Q1 aperture, a tapered SS liner in the MCBX, a TASA SS-copper absorber (1.1-m long, $25 < r < 60$ mm) at 30.45 m from the IP in front of the Q2a quad, a TASB SS-copper absorber (1.2-m long, $33.3 < r < 60$ mm) at 45.05 m from the IP in front of the Q3 quad, and a 3-mm thick beam pipe in the Q2a through Q3 region.

Alternating magnetic field in the quads affects drastically the distribution of energy deposition ϵ in the inner triplet: ϵ peaks in horizontal and vertical planes and reaches maxima at a downstream or/and upstream end of the quads. There is a strong gradient in radial ϵ -behavior. Fig. 12 shows azimuthally integrated isocontours of power density in the region and Fig. 13 shows its azimuthal structure in the Q1 inner coil for the horizontal (baseline) and vertical crossings at the IP.

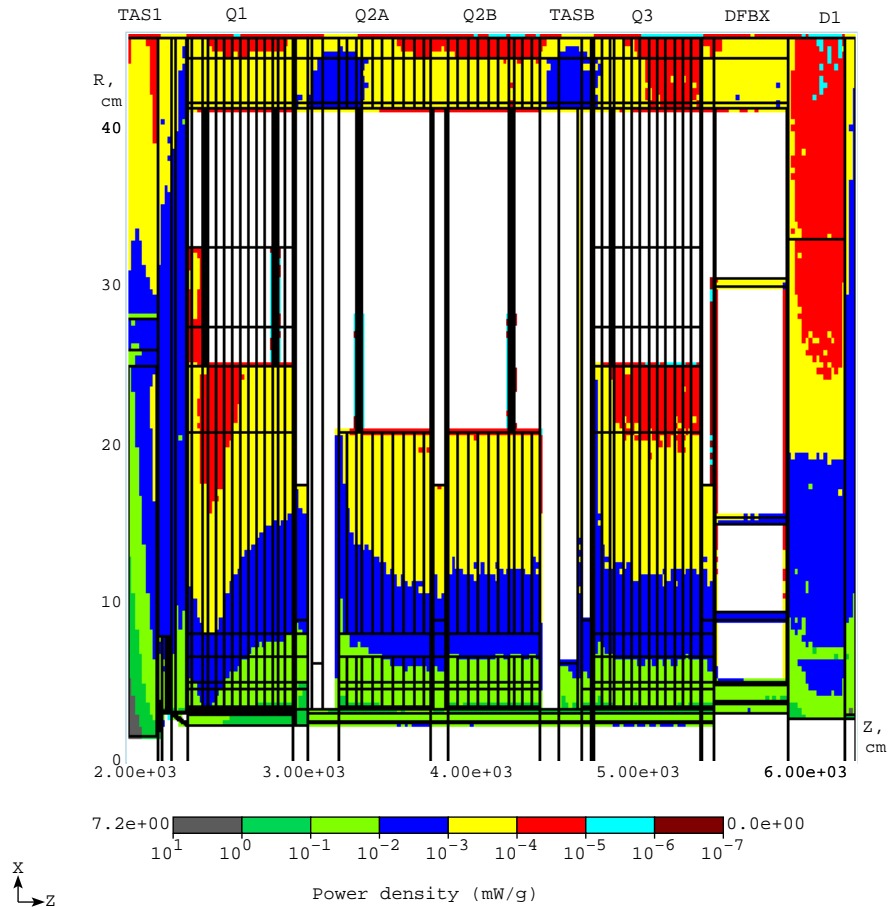


Figure 12: Azimuthally averaged power density isocontours (mW/g) in the IP5 inner triplet.

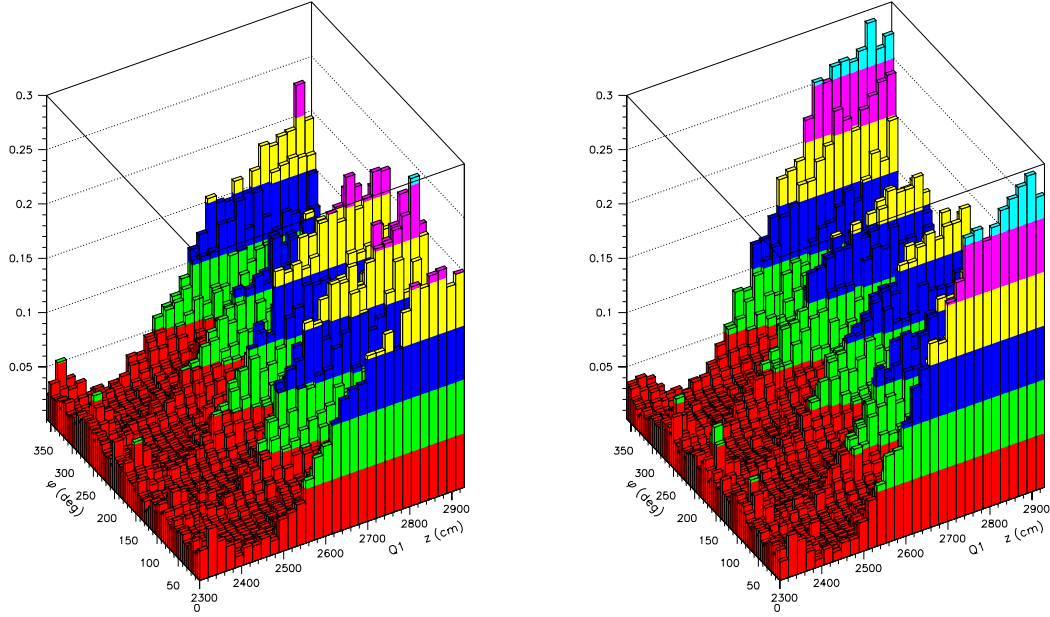


Figure 13: Power density (mW/g) azimuthal structure along the Q1 inner coil for horizontal (left) and vertical (right) crossings in the IP5.

A longitudinal distribution of the azimuthal peak in the first radial bins of the SC coils ($35 < r < 46.5$ mm) in the IP1(R) and IP5(R) inner triplets is shown Fig. 14. These results are applicable to the other sides of the IRs, inverting the IP1(R)-IP5(L) and IP5(R)-IP1(L) pairs. The power density reaches its maximum ϵ_{max} at β_{max} in the Q2b-Q3 region. This value is further increased in Q2b due to horizontal (IP5(R)) and vertical (IP1(L)) crossings. With all of the above protective measures, one can keep ϵ_{max} a factor of two to three—at the baseline luminosity—below the assumed quench limit of 1.6 mW/g. The distribution of power dissipation in the IP5(R) inner triplet is shown in Fig. 14 separately for the coil regions, components inside the bore and for the remaining magnet mass.

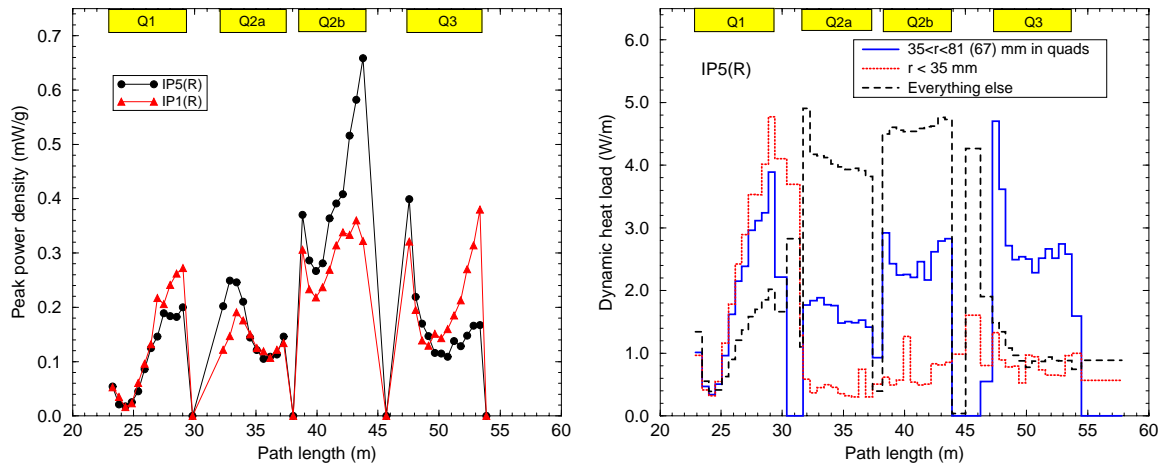


Figure 14: Early design peak power density in the first radial bin of the SC coils ($35 < r < 46.5$ mm) of the IP1 and IP5 inner triplet (left) and power dissipation in the IP5 inner triplet (right).

The absorbers do a very good job intercepting a significant fraction of the energy escaping the collider detectors (see Fig. 15). The TAS alone absorbs 184 W on each side of the IP. The price for that is very high residual dose levels in the TAS and its vicinity (see previous section). Power density distributions in the absorbers TASA and TASB are presented in Fig. 16. The Q1 inner absorber catches about 60% of power in the Q1 region.

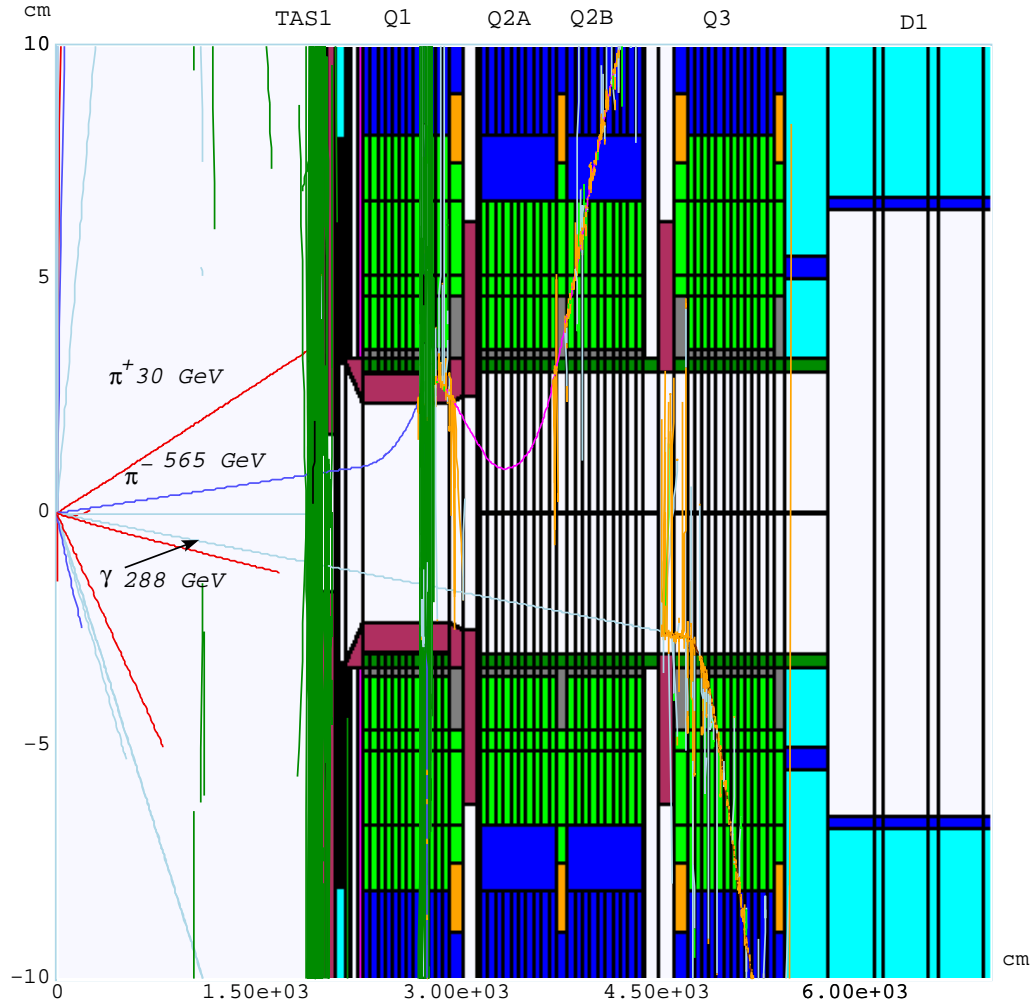
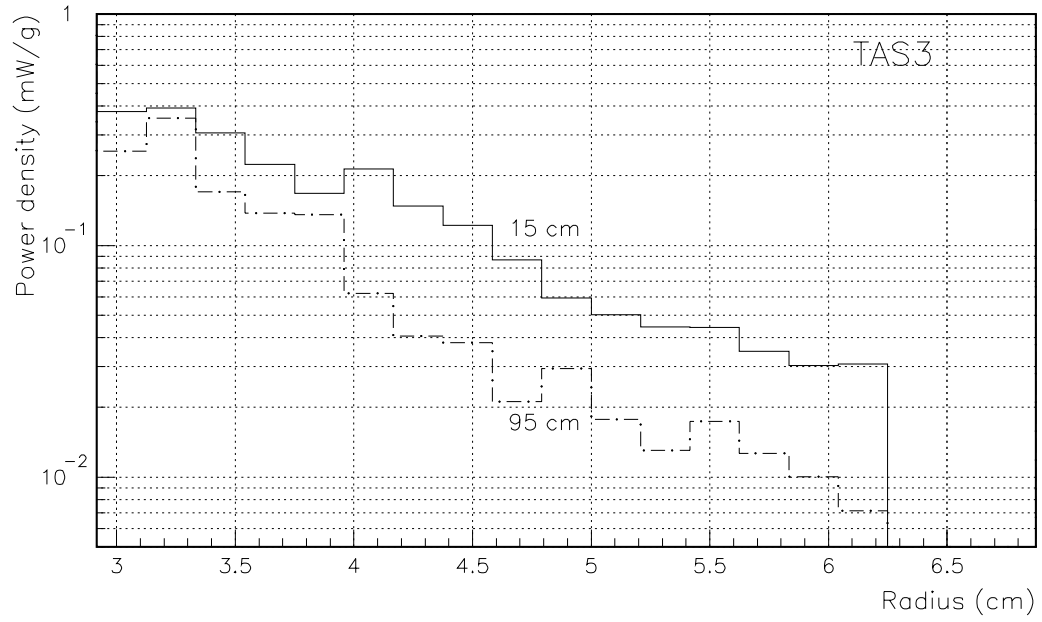
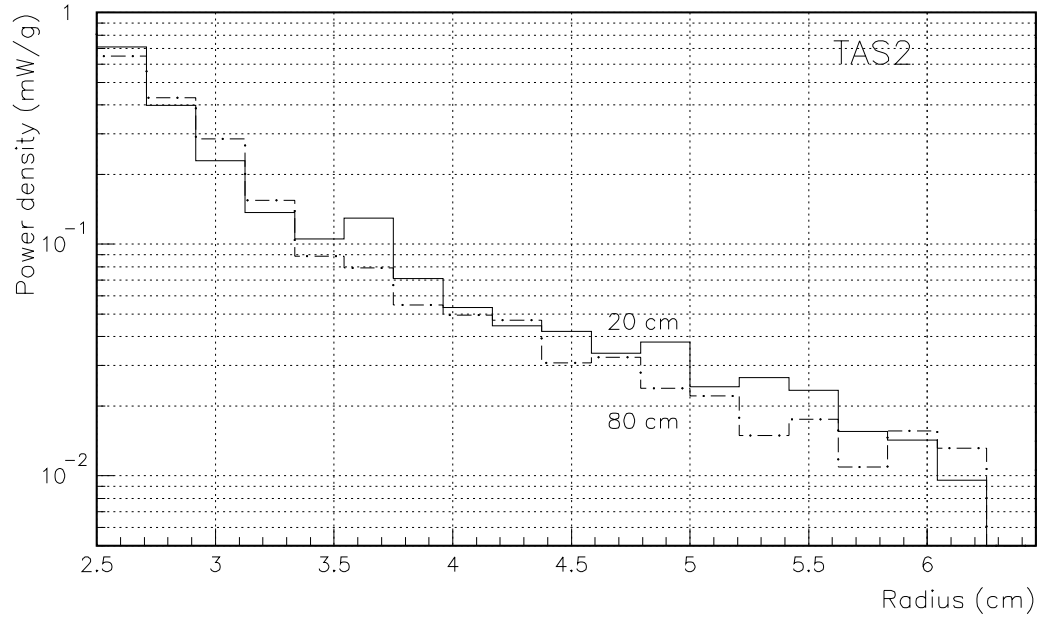


Figure 15: Particle tracks reaching the inner triplet and those generated there for a pp -collision in the IP1.



LHC IP5 at $10^{34} \text{cm}^{-2} \text{s}^{-1}$. Azimuthally averaged power density. MARS14(2000)

Figure 16: Power density vs radius for two longitudinal positions in the absorbers TASA (top) and TASB (bottom) (former TAS2 and TAS3, respectively).

4.2 Slide bearings

To reduce the high dose to the Q1 Teflon slide bearings, protective measures have been proposed and implemented in the cryostat design [19]. From literature, a radiation dose limit for bare Teflon at room temperature is 1 Mrad = 10 kGy. Our previous calculations gave 10 kGy at the first slide bearing in Q1, or 1 year lifetime.

It turns out that radiation streaming through a 2-cm gap around the IP5 TAS ($26 < r < 28$ cm) is especially bad. MARS calculations show that filling this gap with steel plugs reduces the dose at the first slide bearings by a factor of 20. But filling the gap looks unpractical from a detector/shielding maintenance point of view, even with removable plugs for collider operation only. Two other options studied seem to be also not viable: moving the gap to a larger radius of about 35 cm, or making a step-wise gap, at $26 < r < 28$ cm over the first TAS half and say at $28 < r < 30$ cm over the last 0.9 m.

It was found [19] that two 40-cm long stainless steel (SS) masks in Q1 at $z=23.45$ m, $25 < r < 32.5$ cm, ± 10 -degree horizontal on each site do a good job, reducing the peak dose by almost a factor of 10. The final design implements two 60-cm long and ± 15 -degree wide masks in Q1 at $25 < r < 32.5$ cm in front of the first slide bearings. This provides better protection reducing the peak yearly dose D in the slide bearings from 12-15 kGy/yr to 0.5-1.3 kGy/yr in Q1 and from 1.3 kGy/yr to 0.4 kGy/yr in Q2a, providing the lifetime of these components longer than the design 7 years. This is at $N_2=6.22 \times 10^{15}$ non-elastic interactions per year.

4.3 DFBX feedboxes

The DFBX distribution feedboxes are associated with the superconducting magnets at the physics crossings of IP1, IP2, IP5, and IP8. Each IP has separate DFBX's on each side of the crossing point, so eight DFBX are required for construction of the LHC. The DFBX acts as the interface between the superconducting magnets and systems for cryogenics, main and corrector magnet powering, magnet diagnostic and control instrumentation and insulating vacuum. The high-radiation locations are at IP1 and IP5. The materials used in the DFBX are: 316LN bore tubes and beam screens, 304L stainless steel vessels and piping, NbTi superconducting busses with copper stabilizer, BSSCO 2223 High Temperature Superconductor current leads, PEEK low temperature helium gas seals, PEEK insulator blocks in electrical connectors, Kapton bus insulation and Buna N vacuum seals.

Table 1: The heat load P and peak yearly dose D in the IP1/IP5 DFBX elements.

Element	z -region (m)	P (W)	D (kGy/yr)
Pipe	54.45-58.83	0.841	523.2
Bore		1.994	
Helium		0.108	
Jack		0.936	
Ins+vessel		0.488	
$r=9$ cm	54.485-58.795	1.014	74.18
$r=15$ cm		0.470	20.85
$r=30$ cm		0.272	6.074

Radiation loads calculated for the components of the DFBX feedboxes at $54.159 < z < 58.83$ m are given in Table 1. The DFBX design is driven mainly by the various functional requirements, but two areas are affected by radiation concerns. One of these is the low temperature helium gas seal; a conventional cryogenic seal material such as Kel-F was not usable because the seal is located in a radiation environment that prevented the use of Kel-F. It was found that PEEK was a suitable

cryogenic seal and had sufficiently high tolerance to the expected dose. The other area of concern is driven by heat deposition in the bore tube; the heat input required us to surround the 316LN bore tube with a layer of superfluid helium to maintain the bore tube temperature below the required 3 K.

4.4 Towards final design

In the previous configurations, the peak power density in the Q2b quadrupole is below the quench limit of 1.6 mW/g by only a factor of two. Therefore, further studies have been undertaken to decrease the peak value and thus increase the safety margin taking into account more realistic engineering constraints. A number of options have been considered to study various inner triplet configurations: varying the Q1 beam pipe thickness from 3.25 up to 9.8 mm, removing the TASA absorber, going to a Q2/Q3 beam tube immediately at the exit from the Q1/MCBX assembly, making the cold bore tube in the Q1 of a special size (54/66 mm) with a special beam screen (25.5/26.2 mm radius in the round part) *etc.* Fig. 17 shows the optimal and alternative designs for the Q1 beam tube. Fig. 18 presents corresponding longitudinal distributions of power density in first two radial bins of the SC coils. Note that the Q2a peak is now higher, the Q2b peak is reduced from 0.66 to 0.45 mW/g, and the Q3 peaks are down by about a factor of two.

As a result of the variational studies for the current design, the thickness of the beam tube inside the Q1 quad was chosen to be equal to 8.5 mm, with the TASA being removed. This configuration corresponds to the use of cold bore (53 mm ID, 57 mm OD), with a clam-shell absorber outside the cold bore to build up the required thickness. In this case the cold bore plus clam-shell is 1 mm thicker than would be allowed for a simple stainless steel thick wall tube, based on vacuum considerations. The case in which the extra 1 mm is removed and the beam screen, cold bore, and clam-shell absorber assembly is pushed to the largest possible radius is discussed later in this section.

The current plan is that there will be a beam screen in Q1. The model is a simplification in which the ID is equal to the ID of the circular part of the beam screen, the OD is equal to the OD of the thick beam tube, thereby slightly overestimating the amount of material between the beam and the coil. Comparing different runs in which different Q1 beam tube thicknesses were simulated, the overestimate of the material does not affect the results presented below. Within the estimated errors, the peak power density in Q1 depends only on the total thickness of the beam tube and not on precisely where in radius the material is placed. The situation in Q2 is a bit more complicated and depends on both the amount of material and where it is placed upstream of Q2. It follows from Fig. 18 that the current design ensures a safety margin of approximately a factor of three. It represents significant improvement when compared to the initial design with a safety margin of about two.

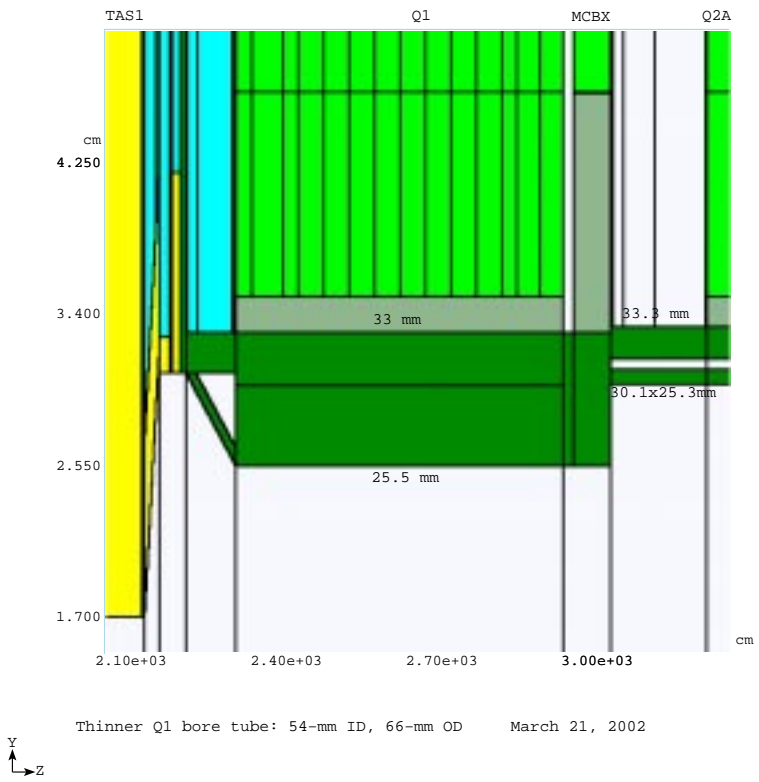
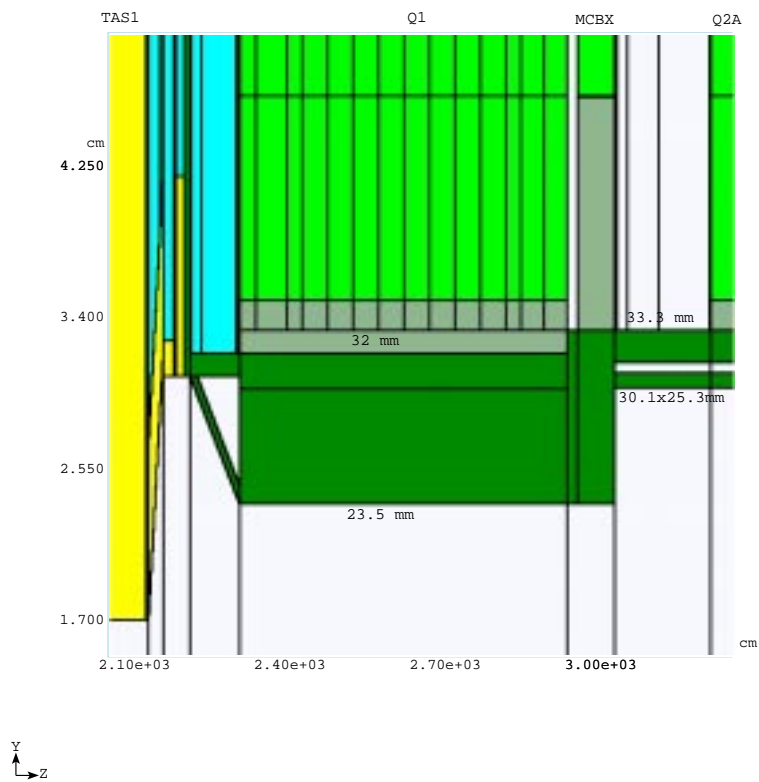


Figure 17: Baseline (top) and alternative (bottom) configurations of the Q1 beam tube.

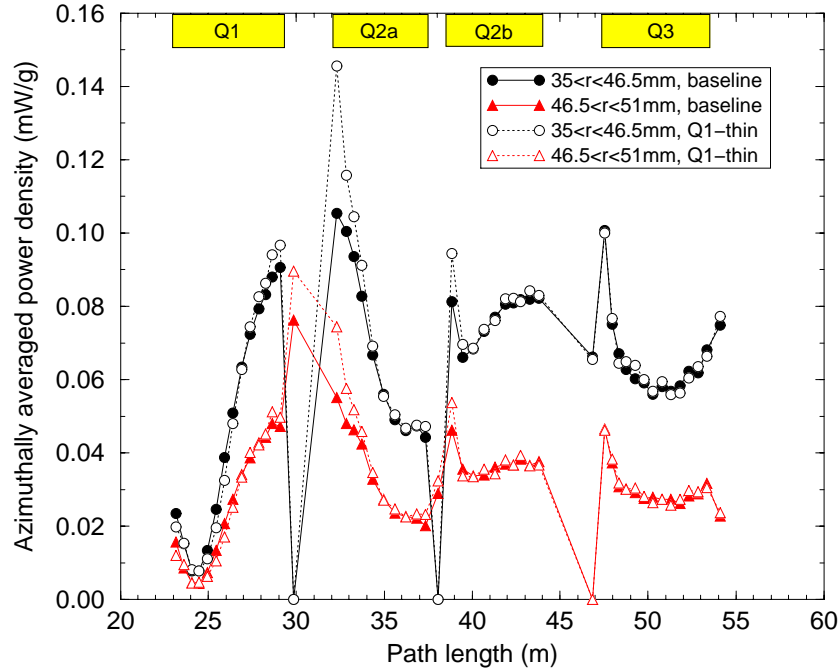
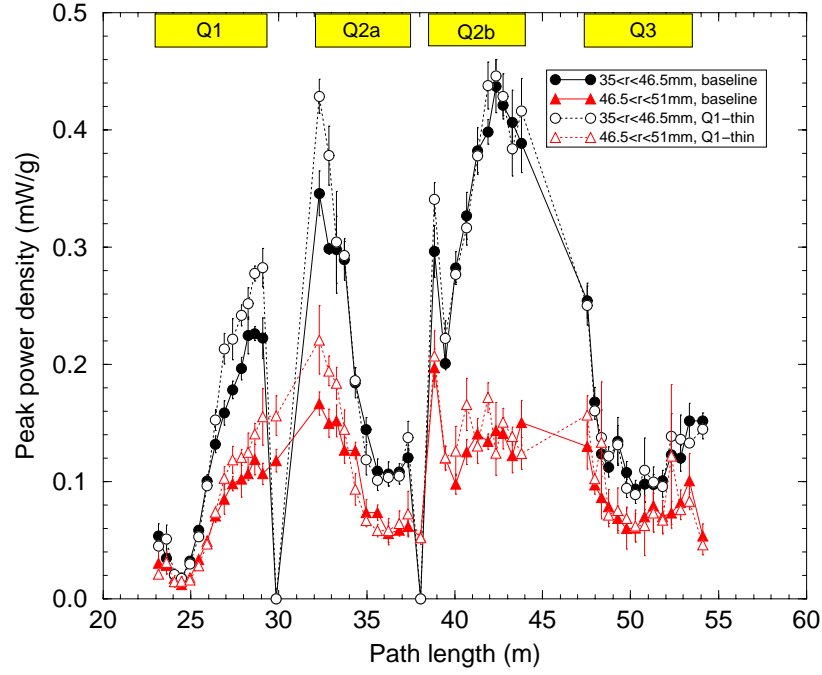


Figure 18: Peak (top) and azimuthally averaged (bottom) power density in the first two radial bins of the IP5 SC quadrupoles for the baseline and alternative designs of the Q1 beam tube shown in previous figure.

The IP5 is designed for a horizontal beam crossing at collisions, while the IP1 – for a vertical one. The beam screens in the Q2a through Q3 are oriented respectively (see Fig. 5(right) and Fig. 19). The crossing plane orientation effects the shape of energy deposition distribution in the inner triplet SC coils, while the peak power density ϵ_{max} in the region is about the same in the IP1 and IP5. Figs. 20 and 21 show azimuthal distributions of power density in the IP5(R) quadrupole coils at the hottest (longitudinally) spots, calculated both for horizontal and vertical crossings. Results are identical within about 1% for the IP1(R) with the crossing plane orientation reversed, i.e., vertical and horizontal crossings, respectively. One sees pronounced peaks in the horizontal and vertical planes, with a difference between maximum and minimum values reaching a factor of 10 and between the peaks and azimuthally averaged values of a factor of 2.5 to 5.5. A longitudinal distribution of an azimuthal peak in the first radial bin of the SC coils ($35 < r < 46.5$ mm) is shown in Fig. 21 (bottom). In the IP5, for the baseline horizontal crossing, the power density reaches its maximum ϵ_{max} at the Q2b non-IP end. For the vertical crossing, there are two equal peaks – at the IP end of Q2a and at the non-IP end of Q3 – which are slightly lower than the one for the horizontal crossing case. In the IP1, the picture is just reversed.

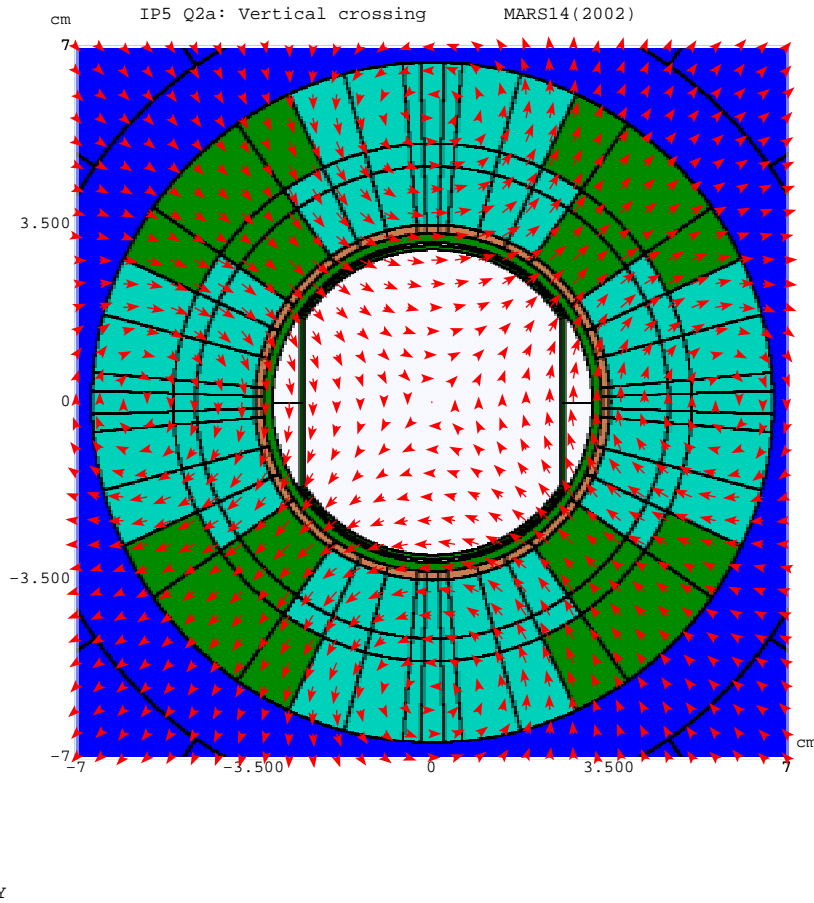


Figure 19: MARS model of the Q2a quadrupole at the IP1 or IP5 with a vertical beam crossing.

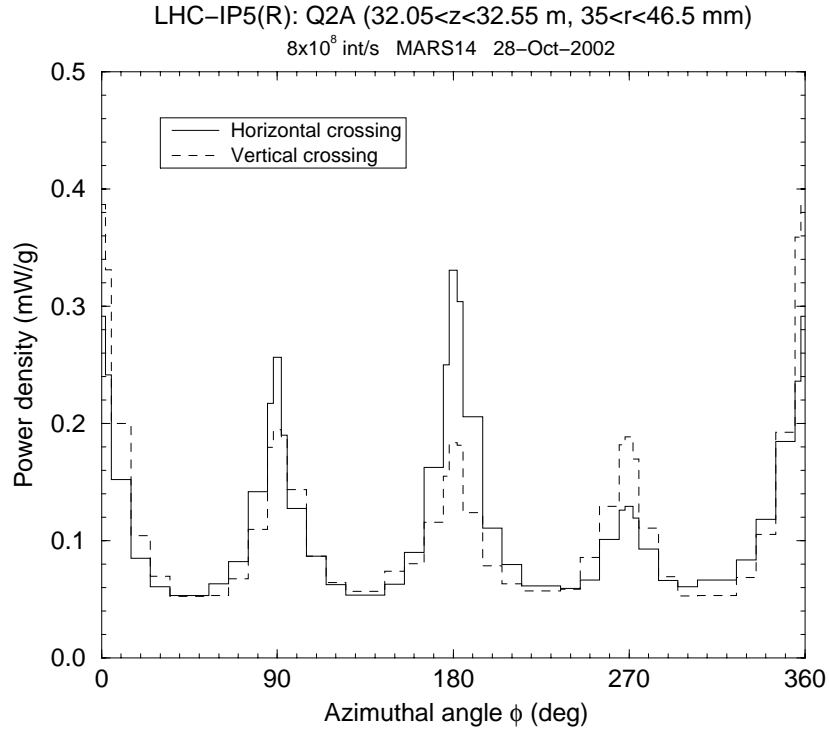
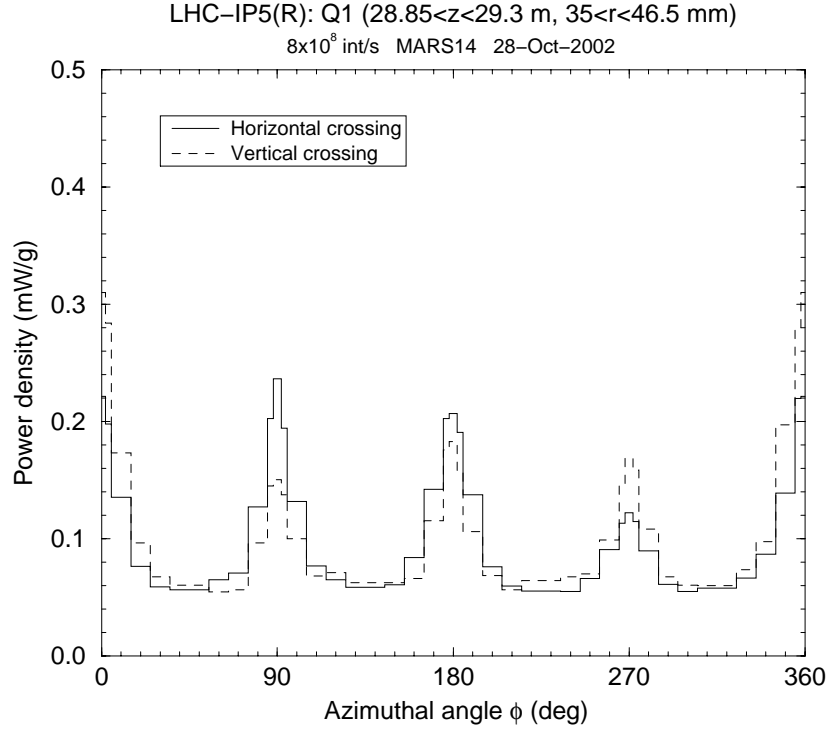


Figure 20: Azimuthal distributions of power density in the first radial bin of the SC coils in the IP5 Q1 (top) and Q2a (bottom) quadrupoles at longitudinal peaks for the horizontal and vertical crossings.

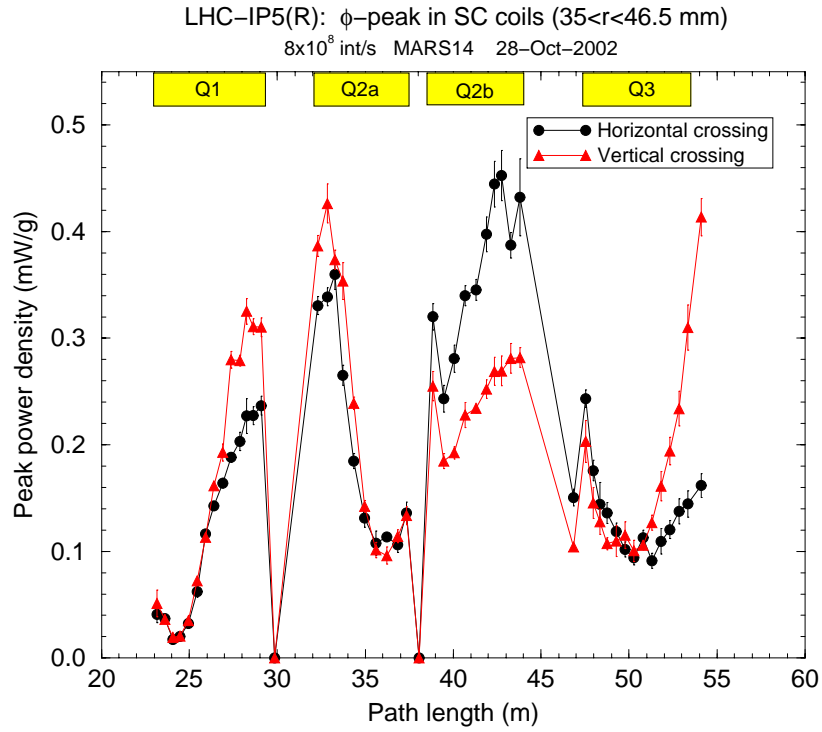
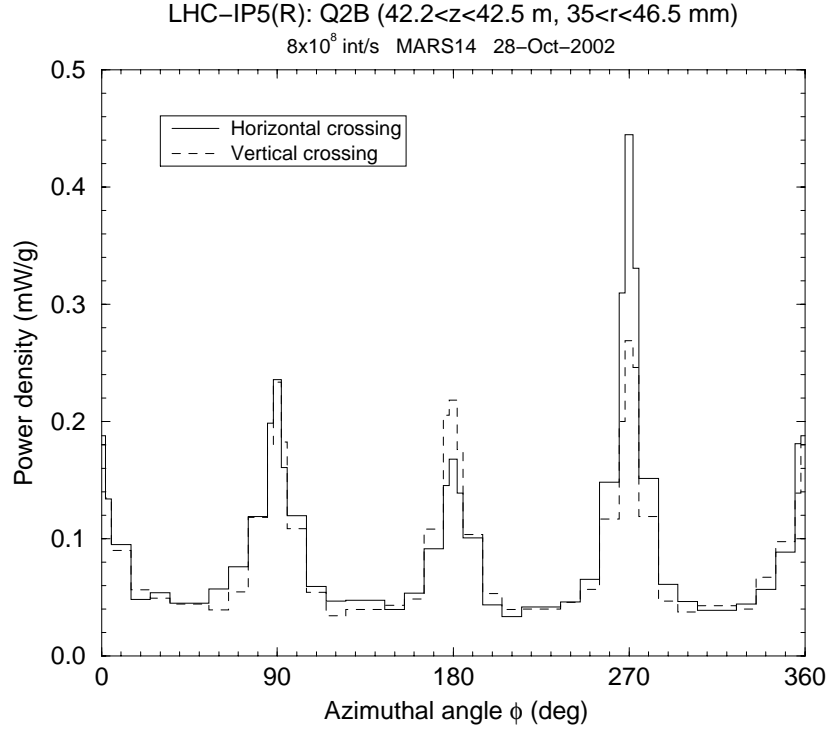


Figure 21: Azimuthal distribution of power density at longitudinal peak in Q2b quadrupole (top) and longitudinal distribution of peak power density (bottom) in the first radial bin of the IP5 SC coils in the IP5 quadrupoles for the horizontal and vertical crossings.

Integral power dissipation in components of the IP5 inner triplet is presented in Fig. 22, while Table 2 gives integral values for the inner triplet region. Statistical uncertainty for each of the values in the Table does not exceed 1%. The integration with respect to radius for all the components listed was performed from 0 up to 45.72 cm, *i.e.* up to the vacuum vessel including the latter. Results for the IP1 are quite similar. The table also gives hadron fluxes and prompt dose on the vessel, useful for a beam loss monitor system design, and an estimate of radiation environment in the tunnel near the cryostat.

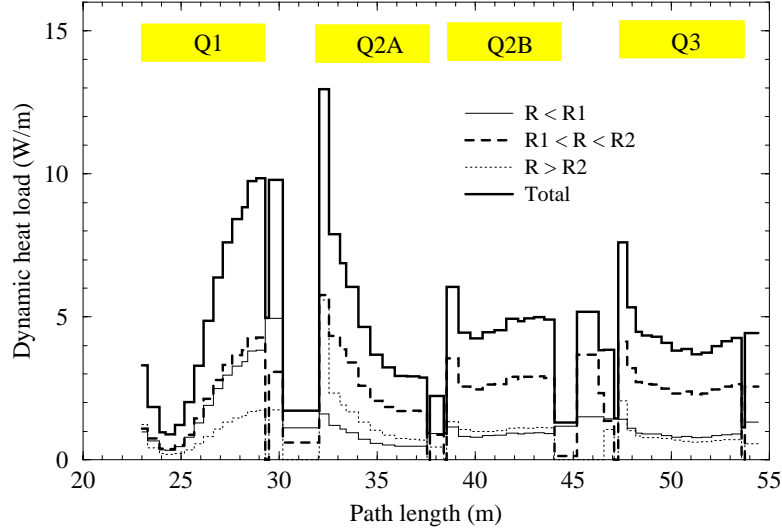


Figure 22: Power dissipation in the baseline IP5 inner triplet components. $R_1=35$ mm, $R_2=81$ mm in Q1 and Q3 and $R_2=67$ mm in Q2a and Q2b.

Table 2: Dynamic heat load P (W) on the IP5 inner triplet components, and prompt dose equivalent DE (Sv/hr) and hadron flux Φ ($10^4 \text{ cm}^{-2} \text{ s}^{-1}$ at $E > 14$ MeV) on the component vessel at longitudinal peaks at the nominal luminosity.

Element	P	DE	Φ
Absorber TAS	184		
Absorber TASB	5.7	18.12	91.84
Quadrupole Q1	30.7	12.44	92.72
Quadrupole Q2a	28.8	22.09	133.4
Quadrupole Q2b	26.6	5.184	40.91
Quadrupole Q3	27.7	12.61	93.76
Corrector MCBX1	6.9	17.55	144.6
Corrector MCBX2	1.6	4.202	32.67
Corrector MQSXA	2.0	15.85	106.0
Corrector MCBXA	3.1	4.712	41.58
Feedbox DFBX	6.92	6.670	39.31
Dipole D1	50		

The alternative design shown in Fig. 17 implies removing the extra 1 mm of the Q1 beam pipe and pushing the beam screen, cold bore, and clam-shell absorber assembly to the largest possible radius. The reduction of the Q1 beam pipe wall thickness by 1 mm and increase of its inner radius by 2 mm increases the peak power density in Q2a by 25% (see Figs. 18 and 23). Therefore, the peak becomes almost as large as that in Q2b, with the safety margin still remaining the same as in the baseline configuration. The calculated peak power density in the second radial bin of both magnets Q1 and Q2a rises faster when compared to that in the first bin. The relatively rapid increase in both radial bins suggests that we should not further reduce the Q1 beam pipe thickness.

The final design implies a 53-mm ID cold bore, with a 57-mm OD. This is built up on the OD to 66 mm with an absorber built around the beam tube. The beam screen is 0.8-mm thick wall, and fits within the ID obviously. It's a non-standard screen the group at CERN will have to make specifically for this location.

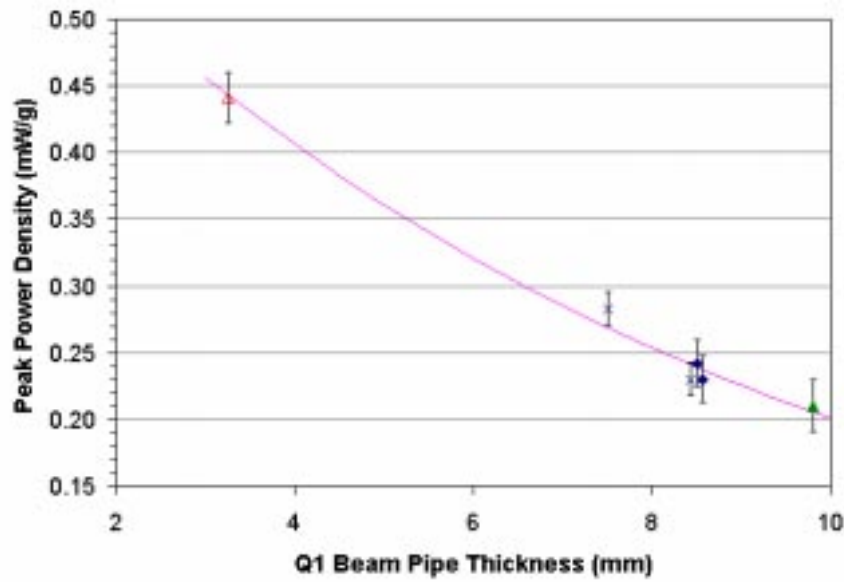


Figure 23: Peak power density in the Q1 inner layer *vs* beam pipe thickness (beam screen together with cold bore).

The dose accumulated in the inner triplet components is quite high (Fig. 24). For the corresponding baseline luminosity profile over an operational year, it can be estimated as D (MGy/yr) = 7.8ϵ (mW/g). The peak in the SC coils $\epsilon_{max}=0.45$ mW/g corresponds then to $D=3.5$ MGy/yr. Averaged over the coils it is about 100 kGy/yr, dropping down to several kGy/yr at the slide bearings supporting the yoke and further down with radius as shown in Figs. 25 and 26.

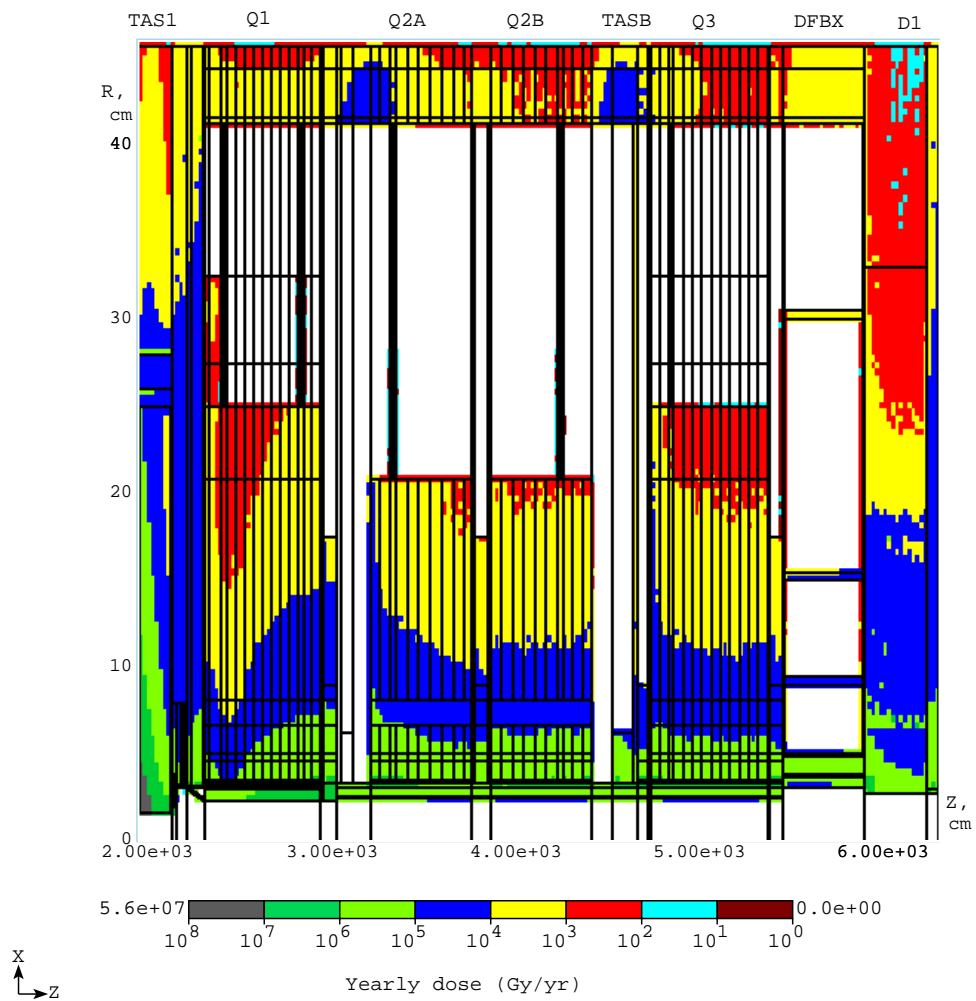
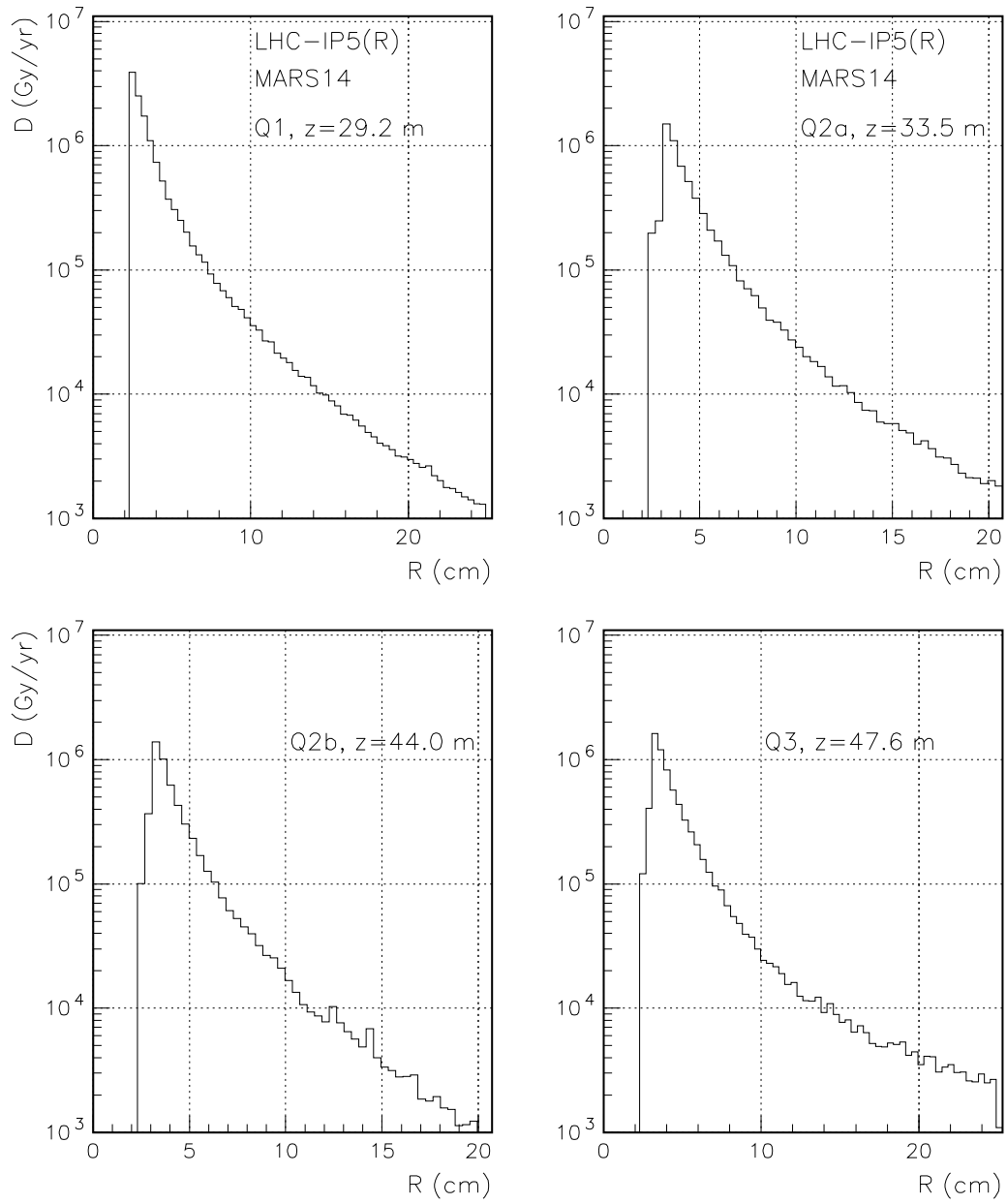
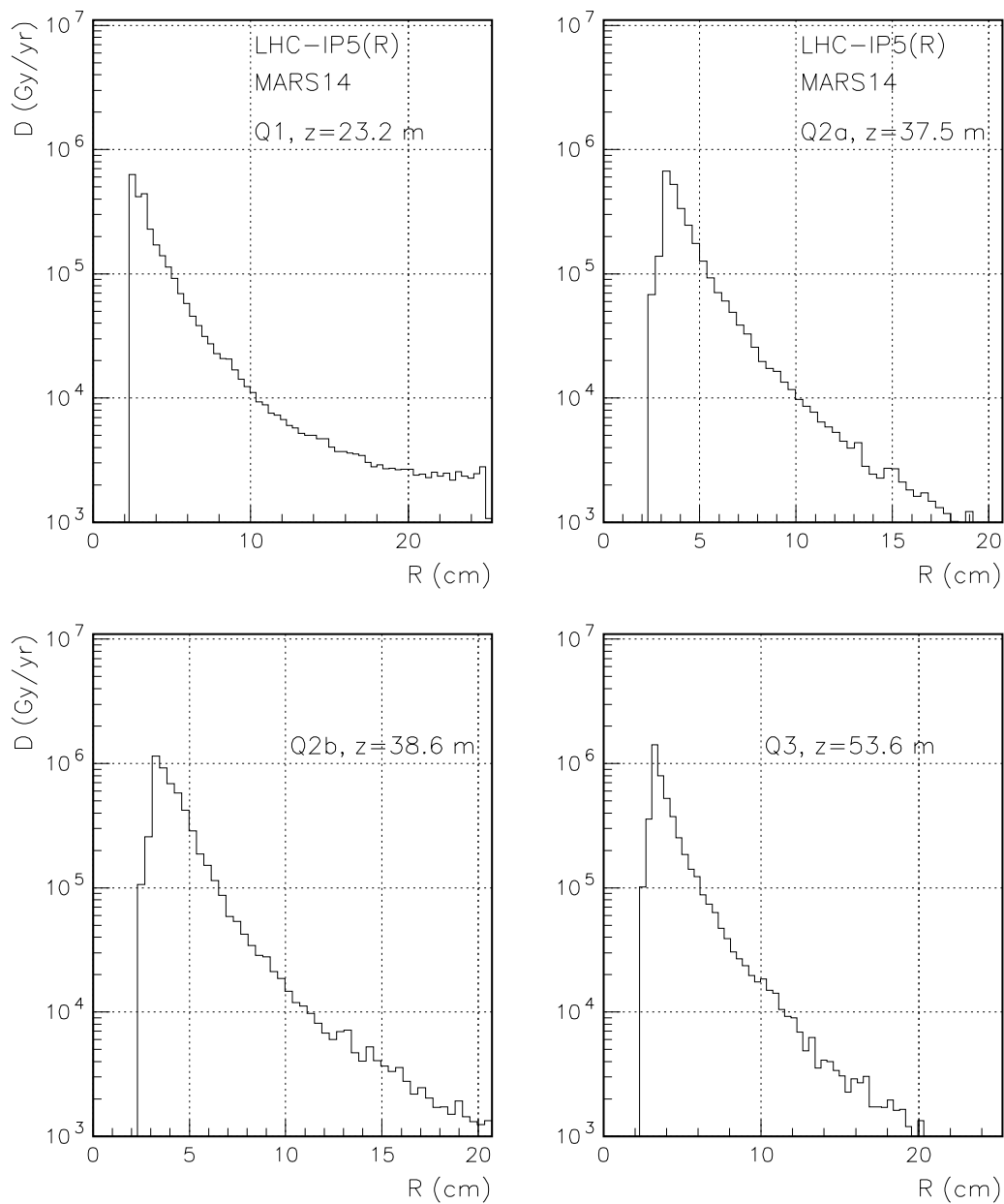


Figure 24: Azimuthally averaged yearly dose (Gy/yr) in the IP5 inner triplet.



LHC IP5(R) azimuthally averaged dose at peaks. MARS14(2002)

Figure 25: Radial distribution of azimuthally averaged dose (Gy/yr) in the IP5 inner triplet at the longitudinal peaks in quadrupoles.



LHC IP5(R) azimuthally averaged dose at thermometers. MARS14(2002)

Figure 26: Radial distribution of azimuthally averaged dose (Gy/yr) in the IP5 inner triplet at the thermometer locations placed at the yoke outer radii.

Residual dose rates are quite significant in the near beam region. After 30-day irradiation and 1-day cooling they are up to several hundred mSv/hr at the TAS and Q1 thick beam tube, up to several tens mSv/hr at the inner parts of the quadrupoles, and below 0.1-0.3 mSv/hr on contact at the vacuum vessel (Figs. 27 and 28(left)). The dependencies of these rates on irradiation and cooling times are shown in Fig. 28(right)) for the IP5 quadrupoles.

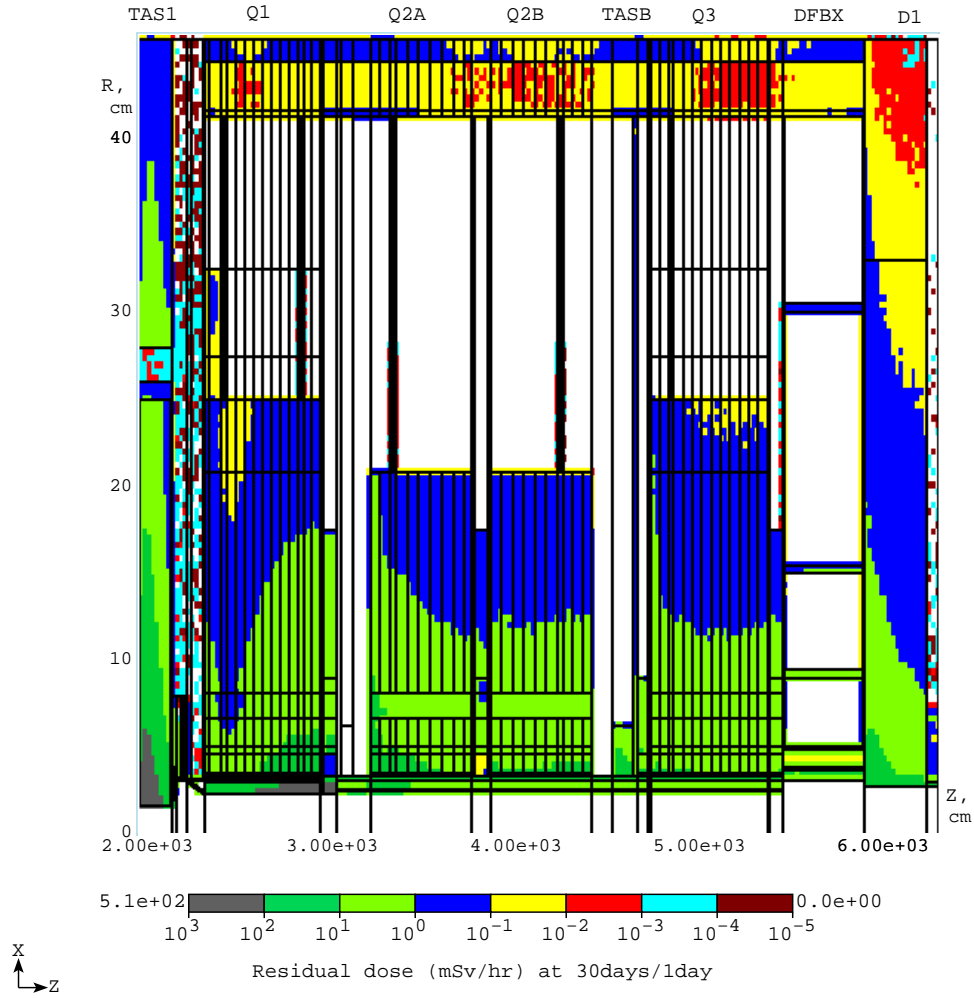


Figure 27: Azimuthally averaged residual dose rate (mSv/hr) on the IP5 inner triplet components after 30-day irradiation and 1-day cooling.

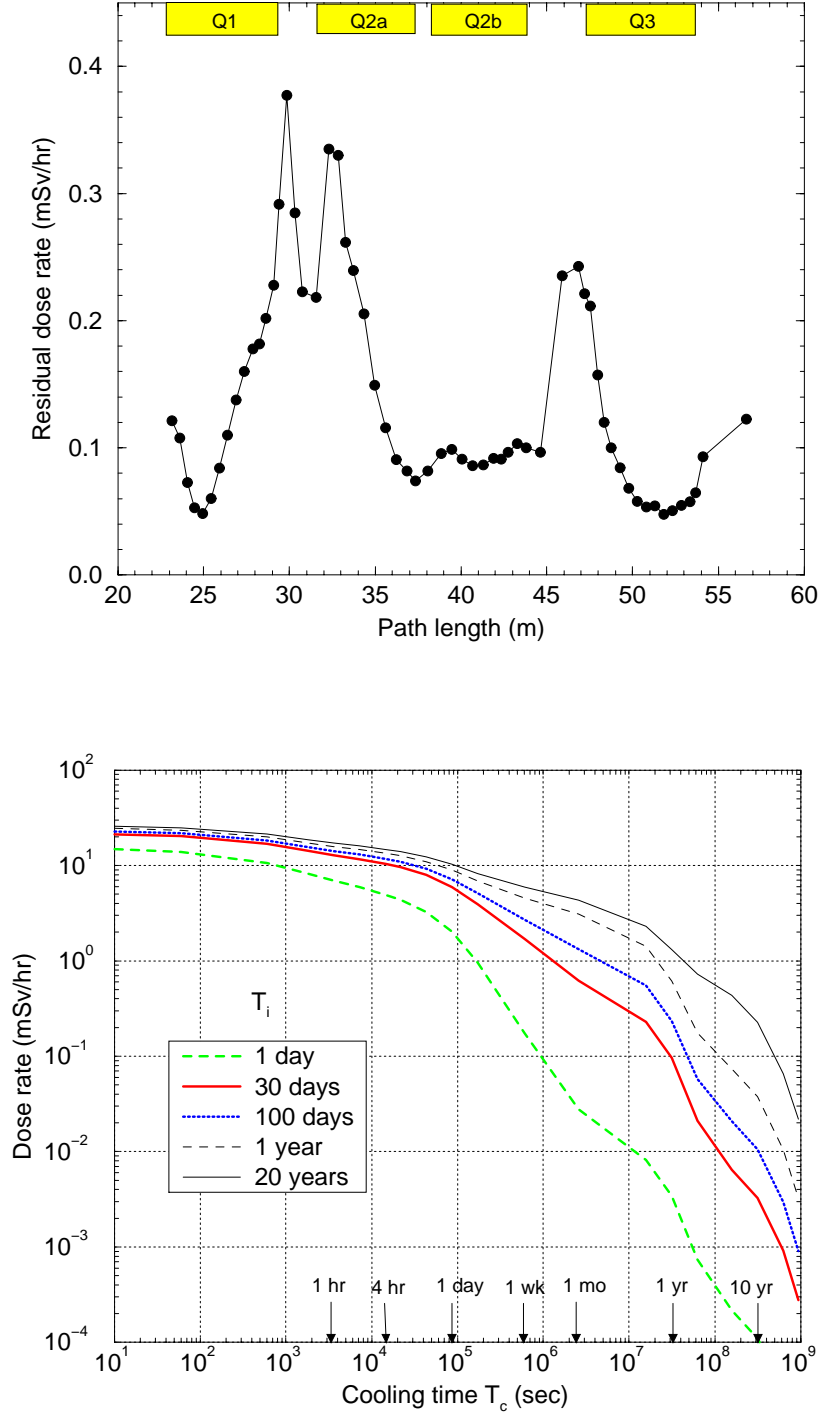


Figure 28: Residual dose rate (mSv/hr) on the IP5 inner triplet vacuum vessel after 30-day irradiation and 1-day cooling (top) and residual dose averaged over the IP1/IP5 quadrupole SC coils (all quads, all layers) vs irradiation and cooling times (bottom).

5 TAN, D2 and Outer Triplet

5.1 Neutral particle absorber TAN

A neutral particle absorber TAN at 140 m on each side of the IP (Fig. 29), is designed to protect the separation dipoles D2 and the outer triplet quads [22]. Its parameters were optimized based on detailed MARS14 calculations. An instrumented copper core ($21 \times 26 \times 350$ cm) with two 5 cm diameter beam holes is surrounded by massive steel shielding with a 30-cm steel / 30-cm marble albedo trap (Fig. 30(top)).

2-D distribution of hadron flux just upstream of the IP5 TAN is presented in Fig. 30(bottom). Due to beam crossing at the IP, a neutral particle centroid is shifted by about 21 mm horizontally (IP5) or vertically (IP1). A splash at the pipe (at 120 mm) is due to low-energy charged hadrons (mainly protons and pions) deflected by the D1 magnet. Fig. 31 shows isocontours of hadron flux and yearly dose at shower maximum of 17 cm in the TAN core. Characteristics of the source term at the TAN are described in Table 3 that gives average values of flux, energy and power coming to the absorber. The incoming power fluxes (predominantly photons) are cut by different components placed between the IP and TAN: by D1 dipoles, vertically at ± 46 mm = ± 27 mm \times (140 m / 82 m); by the inner triplet aperture, at $R \simeq 76$ mm = 30 mm \times (140 m / 55 m); by the TAS aperture, at $R \simeq 112$ mm = 17 mm \times (140 m / 21.25 m).

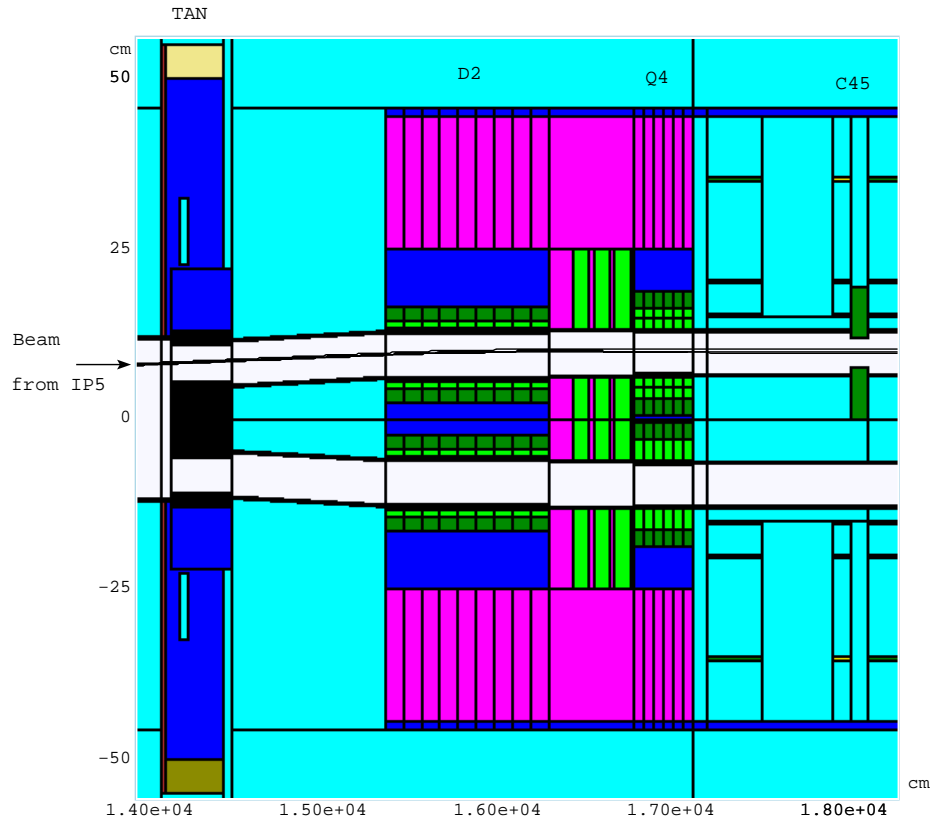


Figure 29: MARS model of the IP5 TAN-D2-Q4 region with TCL (C45) collimator.

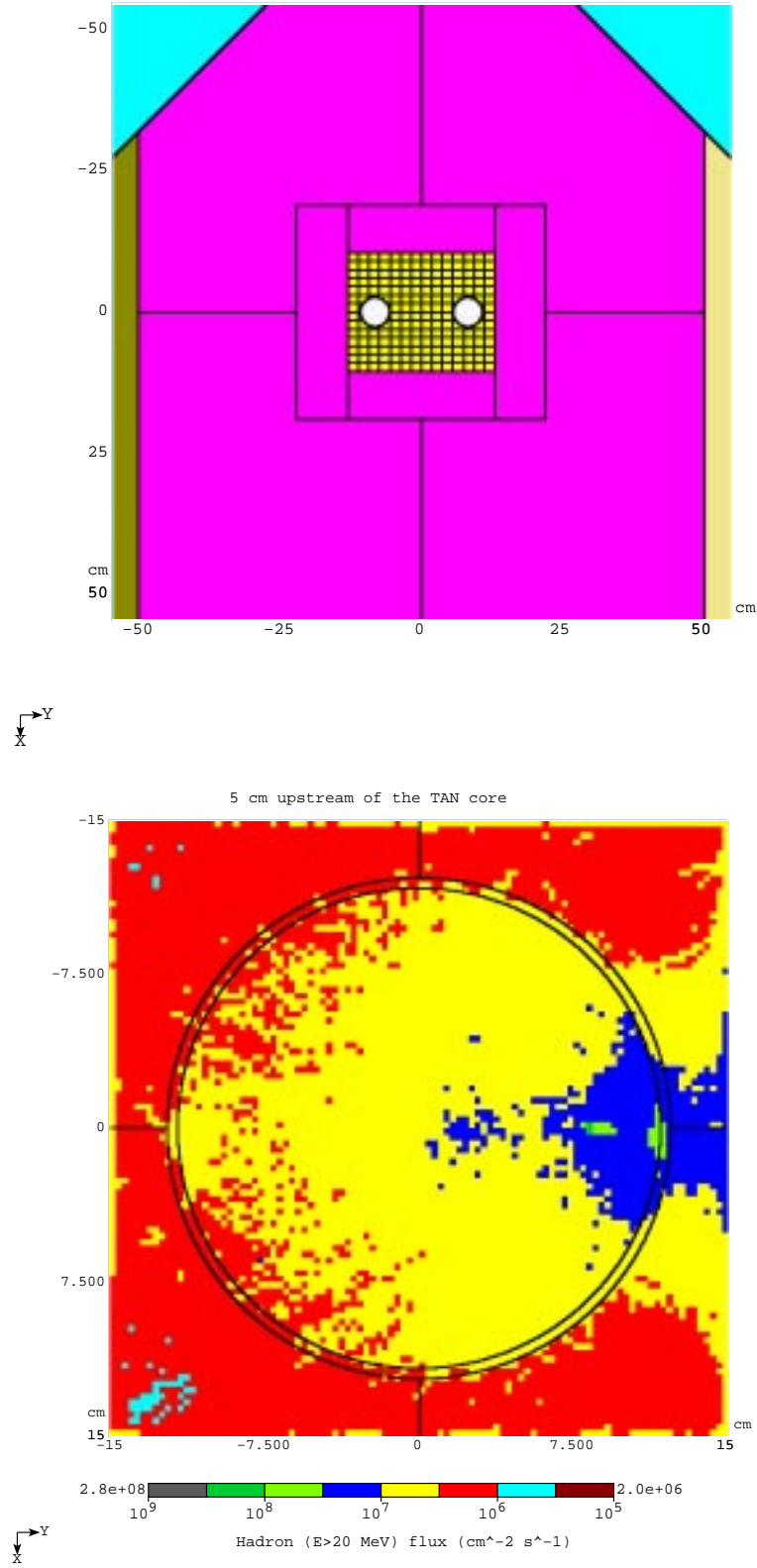


Figure 30: Cross section of the MARS model of the IP5 TAN (top) and 2-D distribution of incoming hadron flux at the TAN core (bottom).

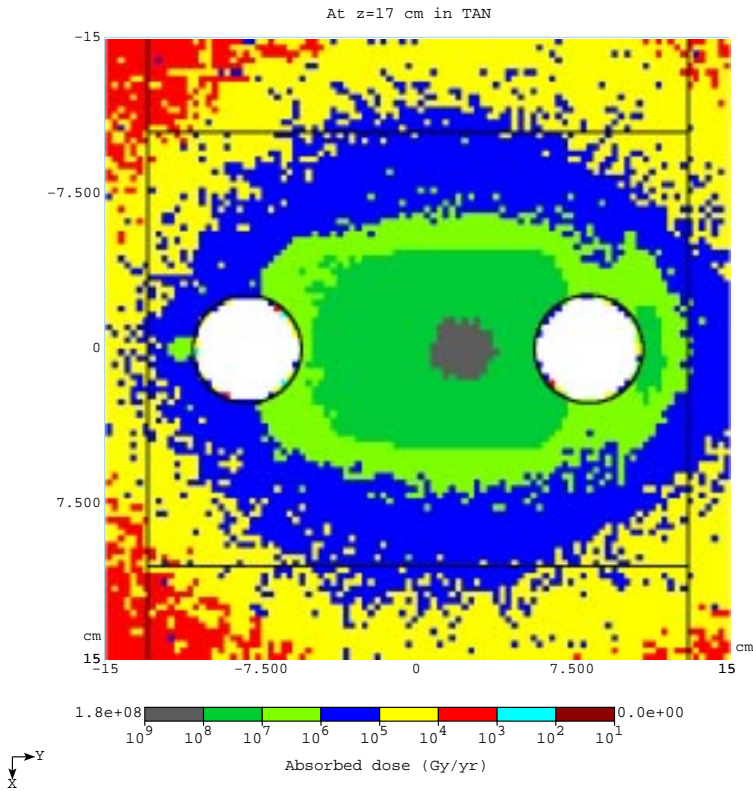
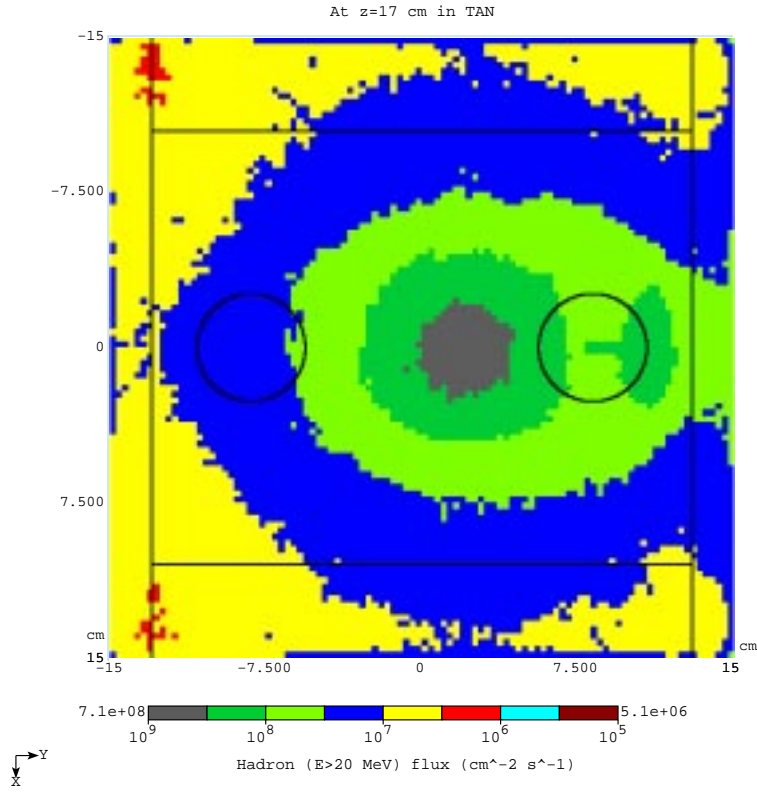


Figure 31: Isocontours of hadron flux in $\text{cm}^{-2}\text{s}^{-1}$ (top) and yearly accumulated dose in Gy/yr (bottom) at 17-cm depth in the IP5 TAN.

Table 3: Average number of particles \bar{N} , energy \bar{E} (GeV), and particle energy \bar{E}/\bar{N} (GeV) per pp collision as well as particle flux ϕ_{tot} ($cm^{-2}s^{-1}$) and total power flux P_{tot} (W) in front of the IP5 TAN. “Aperture” stands for a 50-mm diameter hole for the outgoing beam.

Region	Value	p	n	$\pi^{\pm}K^{\pm}$	γ	e^{\pm}	μ^{\pm}	P_{tot}
Aperture	\bar{N}	0.148	0.027	0.125	28.4	2.74	$3.0^{*)}_4$	124
	\bar{E}	887	19.3	33.1	29.7	1.14	1.3_{-2}	
	\bar{E}/\bar{N}	6014	726	266	1.05	0.417	42.5	
	ϕ_{tot}	5.6_{+6}	1.2_{+6}	4.7_{+6}	1.1_{+9}	1.2_{+8}	1.2_{+4}	
TAN core less aperture	\bar{N}	0.109	0.479	0.875	301	24.5	0.006	199
	\bar{E}	102	726	56.8	662	7.20	0.031	
	\bar{E}/\bar{N}	938	1516	64.8	2.20	0.294	4.87	
	ϕ_{tot}	2.5_{+5}	1.2_{+6}	1.8_{+6}	6.8_{+8}	5.3_{+7}	1.4_{+4}	
Coll.box	\bar{N}	0.133	0.464	0.826	197	14.0	0.016	4.7
	\bar{E}	15.8	0.854	15.0	3.36	1.46	0.123	
	\bar{E}/\bar{N}	118	1.84	18.2	0.017	0.104	7.53	
	ϕ_{tot}	1.0_{+5}	4.4_{+5}	5.5_{+5}	1.4_{+8}	1.1_{+7}	1.1_{+4}	
Shielding	\bar{N}	0.331	1.66	1.72	460	32.1	0.109	4.3
	\bar{E}	1.88	1.57	22.4	5.46	1.98	0.510	
	\bar{E}/\bar{N}	5.68	0.943	13.0	0.012	0.062	4.67	
	ϕ_{tot}	3.1_{+4}	2.0_{+5}	1.4_{+5}	4.2_{+7}	3.2_{+6}	8.9_{+3}	
Tunnel (air)	\bar{N}	1.14	7.08	4.33	1390	107	0.714	6.7
	\bar{E}	2.08	2.24	25.7	15.2	5.49	1.93	
	\bar{E}/\bar{N}	1.82	0.316	5.94	0.011	0.051	2.70	
	ϕ_{tot}	1.4_{+4}	1.1_{+5}	4.7_{+4}	1.6_{+7}	1.5_{+6}	7.8_{+3}	
Total	\bar{E}	1009	750	153	716	17.3	2.6	339

*) Read as 3.0×10^{-4} .

Shower maximum in the TAN takes place at $15 < z < 20$ cm, $-1.5 < x < 1.5$ cm, and $1.86 < y < 3.71$ cm, where x is up and y is to the right. Maximum particle fluxes ($E > 0.1$ MeV) at the longitudinal peak in the IP1/IP5 TAN absorbers in $cm^{-2}s^{-1}$ are 3.2×10^9 for neutrons, 3.6×10^8 for charged hadrons, 8.1×10^{11} for photons, 5.8×10^{10} for electrons and 1.3×10^6 for muons.

Energy and angular distributions of incoming particles at the IP5 TAN are presented in Figs. 32 through 34. Muon component is not shown because of its negligible contribution when compared to the other particles (see Table 3). The distributions of incoming particles can be useful to determine optimal arrangement of detectors used in the instrumented TAN core [21]. Difference between IP1 and IP5 reveals itself mostly as the 6%-difference in power of radiation entering the region (318 and 339 W for IP1 and IP5, respectively). For both IP1 and IP5 the most energetic particles in this region are protons with average energy of about 6 TeV observed in the aperture for the outgoing beam. Particle distributions inside the IP5 TAN core and at shower maximum (20 cm) are given in Fig. 32. A build-up in the TAN core is quite substantial: peak power density reaches 22.5 mW/g or 180 MGy/yr at shower maximum at 17 cm in the core. The power dissipated in the core is 176 W (see Table 4) and is brought mostly by energetic neutrals generated at the IP and generated by secondaries in the near beam components on the 140-m way from the IP.

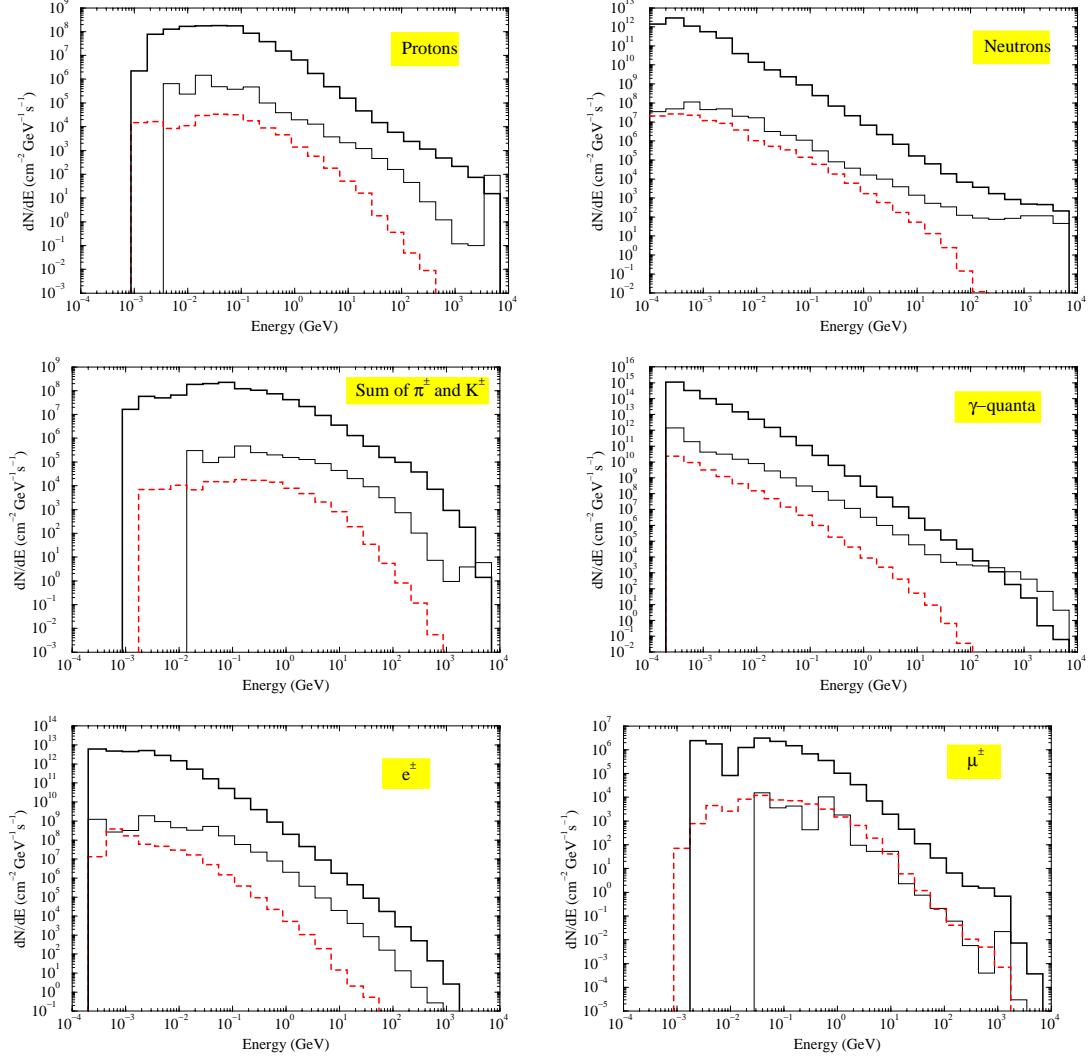


Figure 32: Particle energy spectra in front of the TAN at $z=139$ m (thin and dashed histograms) and at shower maximum in the TAN at $z=141.4$ m (thick histogram). Thick line is for $40 \times 40 \text{ mm}^2$ area, thin line is for spectra averaged over the TAN core, and dashed line is that averaged over the tunnel (without the TAN and its shielding).

Table 4: Integral power dissipation P in some of the IP5 outer triplet components at nominal luminosity. Statistical error is 2-3%.

Object	TAN core	TAN total	D2 coil	Q4 coil	Q5 coil
P (W)	176	189	0.42	0.16	0.82

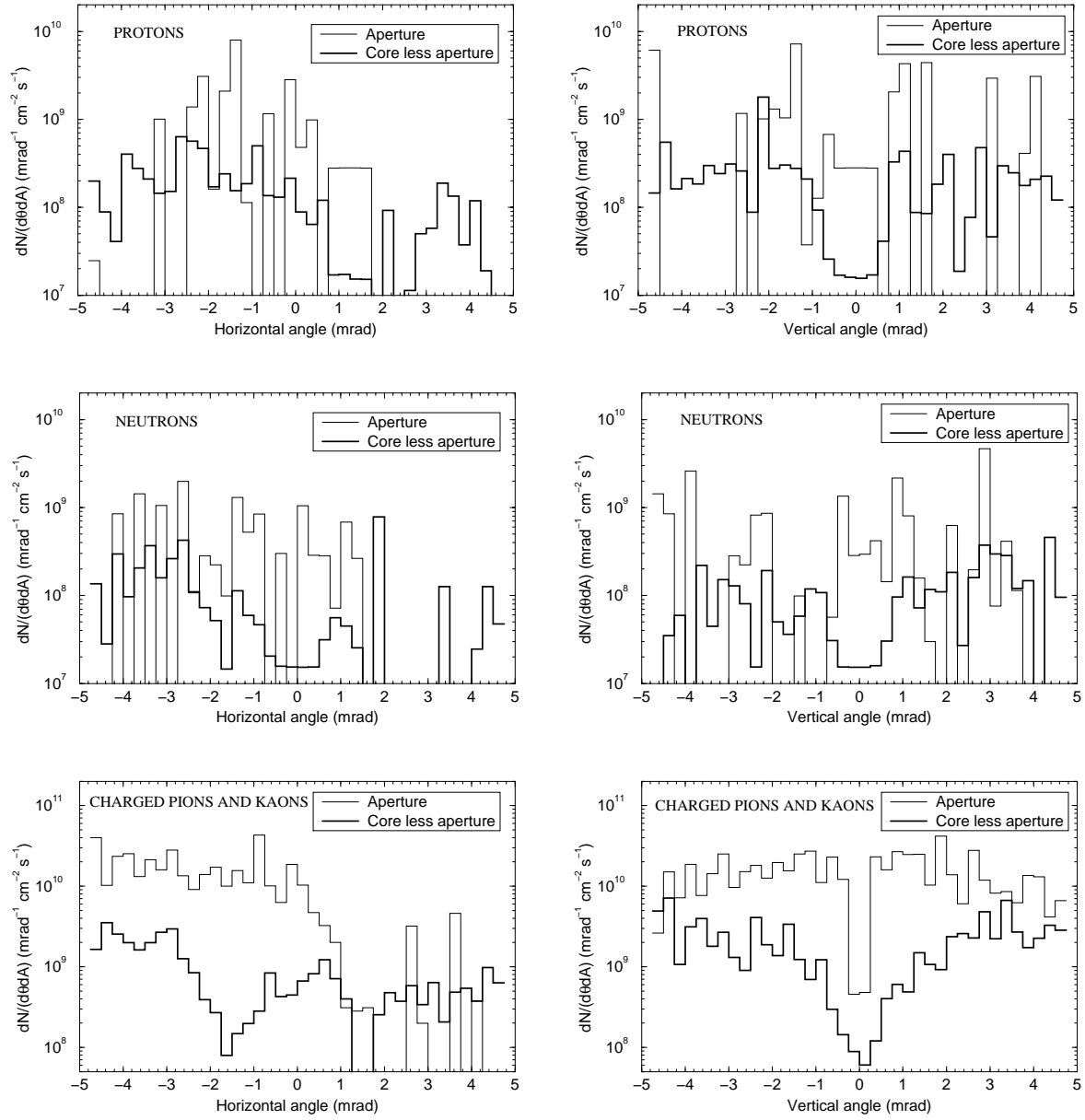


Figure 33: Hadron distributions vs projected angles in front of the TAN (z=139 m). Zero angle corresponds to the TAN axis. “Aperture” means the 50-mm hole in the TAN for the beam going from the IP5 and “Core less aperture” means a cross section of the TAN copper core minus the hole.

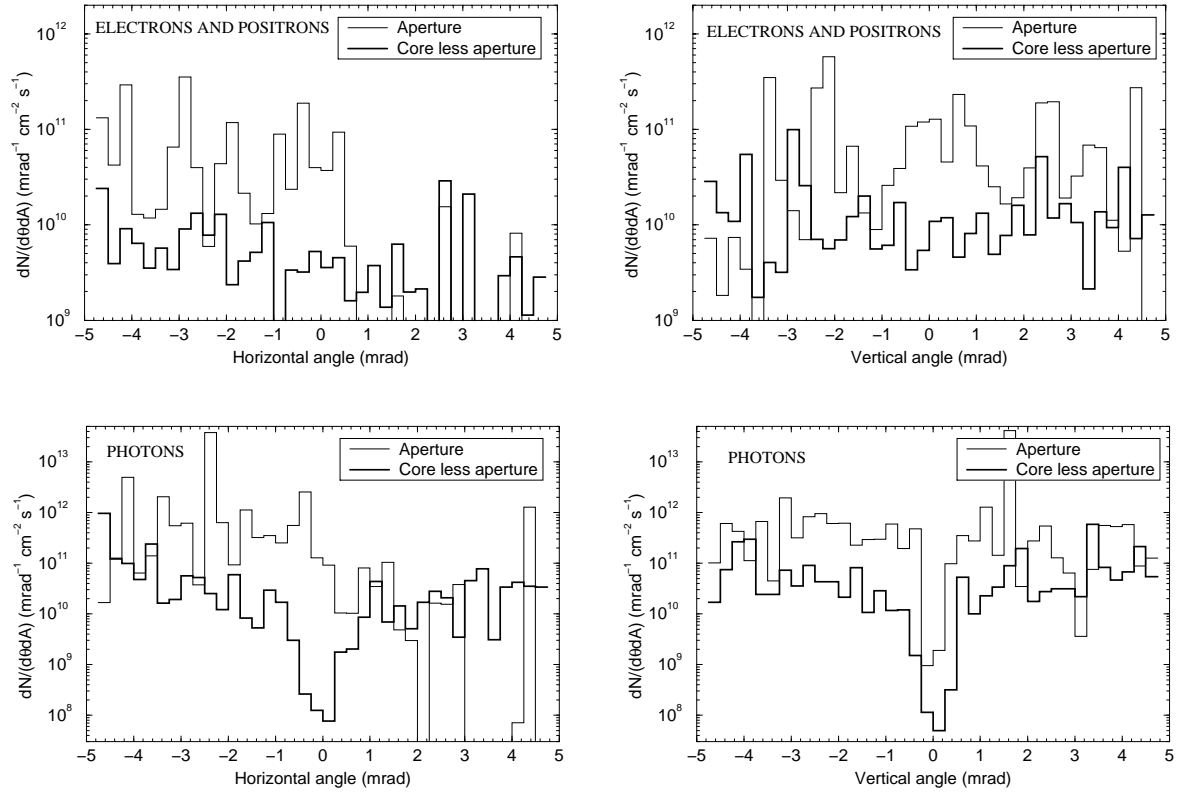


Figure 34: Electron, positron, and photon angular distributions vs projected angles in front of the TAN ($z=139$ m). Zero angle corresponds to the TAN axis.

Table 5: Average number of particles \bar{N} , energy \bar{E} (GeV), particle energy \bar{E}/\bar{N} (GeV) per pp collision, and total power flux P_{tot} (W) and particle flux ϕ_{tot} ($cm^{-2}s^{-1}$) at $8 \cdot 10^8$ interaction/s, at shower maximum. “CdTe” stands for a luminosity monitor – a $40 \times 40 mm^2$ luminosity measuring detector.

Region	Value	p	n	$\pi^\pm K^\pm$	γ	e^\pm	μ^\pm	P_{tot}
Aperture	\bar{N}	0.421	22.9	0.966	1760	53.4	4.5^{+*}_{-3}	122
	\bar{E}	856	21.4	32.1	37.1	3.02	1.7_{-3}	
	\bar{E}/\bar{N}	2030	0.935	33.3	0.021	0.057	0.37	
	ϕ_{tot}	2.0_{+7}	1.7_{+9}	4.6_{+7}	1.0_{+11}	3.3_{+9}	2.1_{+5}	
CdTe detector at shower maximum	\bar{N}	0.870	29.6	4.99	10920	738	0.017	52
	\bar{E}	17.5	130	108	101	48.9	0.050	
	\bar{E}/\bar{N}	20.1	4.40	21.5	0.009	0.066	2.98	
	ϕ_{tot}	5.7_{+7}	2.9_{+9}	2.8_{+8}	7.0_{+11}	5.5_{+10}	9.0_{+5}	
TAN core less aperture and CdTe	\bar{N}	2.64	364	11.4	24370	1470	0.072	78
	\bar{E}	48.6	138	172	174	75.5	0.090	
	\bar{E}/\bar{N}	18.5	0.380	15.0	0.0071	0.051	1.26	
	ϕ_{tot}	7.7_{+6}	1.5_{+9}	2.9_{+7}	7.8_{+10}	5.7_{+9}	1.9_{+5}	
Total	\bar{E}	922	290	311	312	127	0.1	251

*) Read as 4.5×10^{-3} .

Table 5 shows particle flux and other integral quantities at shower maximum in the TAN core, at 20-cm depth (141.4 m downstream of IP). In contrast to the upstream end of the TAN, shower energy in this cross-section (except the aperture) is distributed almost uniformly between nucleons, mesons, and leptons.

Residual dose rate on contact at the outer surface of the TAN steel shielding ($y=+55$ cm in Fig. 30) is shown in Fig. 35 for irradiation from 1 day up to 20 years continuously as a function of cooling time. In realistic operation, the dose is below 0.2 mSv/hr about a day after shutdown. It ensures safe hands-on maintenance in the vicinity of the TAN.

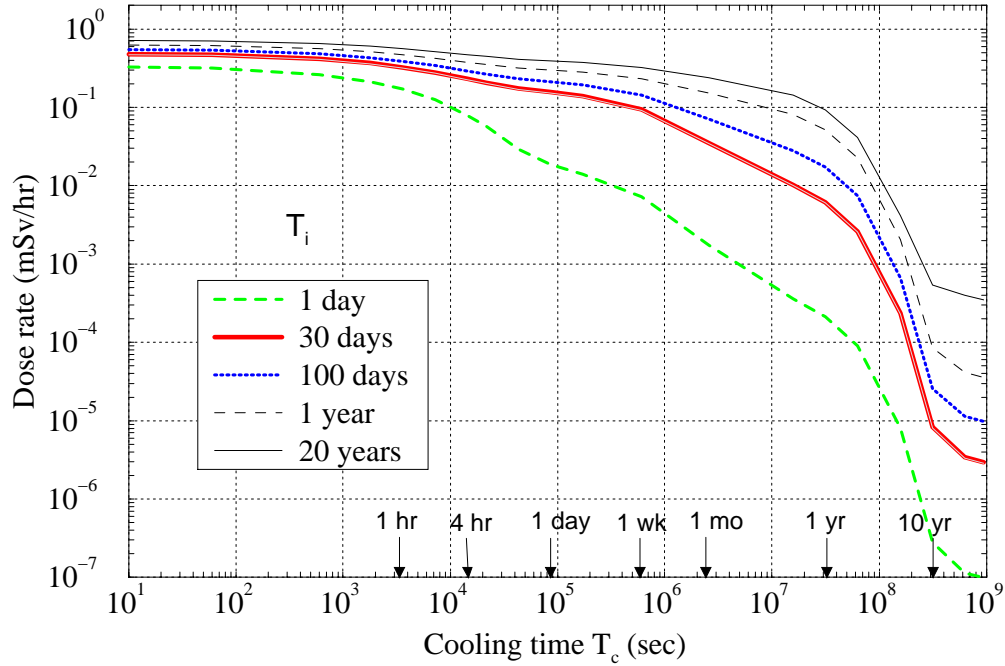


Figure 35: Residual dose (mSv/hr) averaged over the TAN aisle side vs cooling time.

5.2 Radiation in TAN-D2 transition

Transverse radiation isocontours at 30-cm and 55 cm depths in the TAN, its shielding and tunnel cross-section are presented in Figs. 36 through Figs. 38.

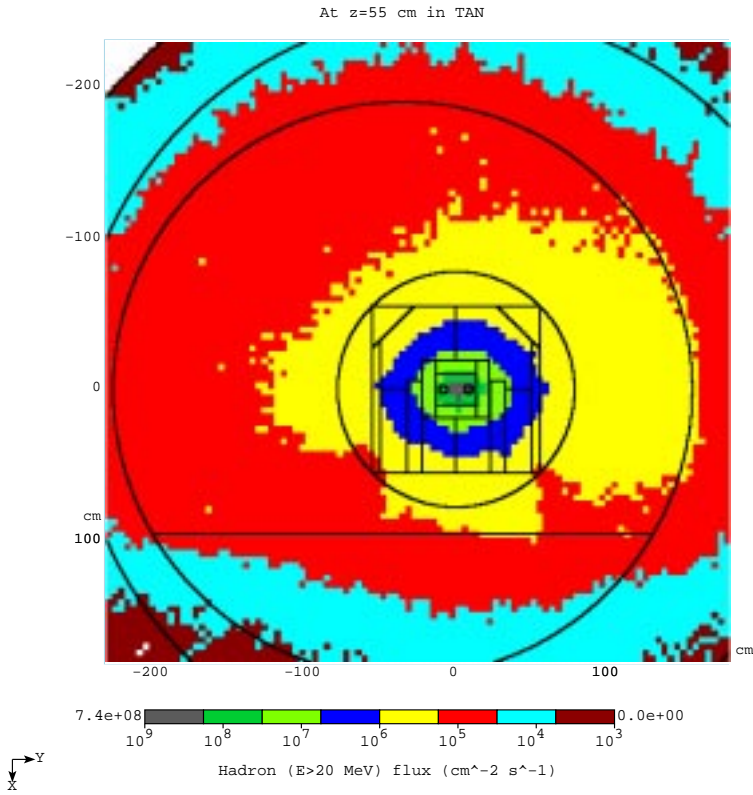
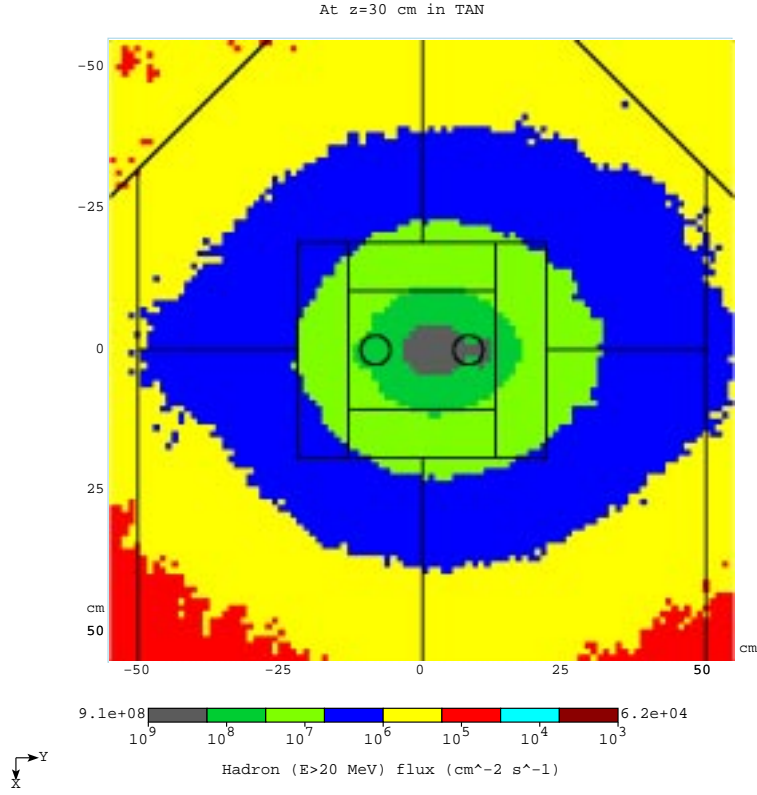


Figure 36: Hadron ($E>20$ MeV) flux ($\text{cm}^{-2}\text{s}^{-1}$) isocontours in the TAN and around at 30 cm (top) and 55 cm (bottom) from the entrance to the TAN core.

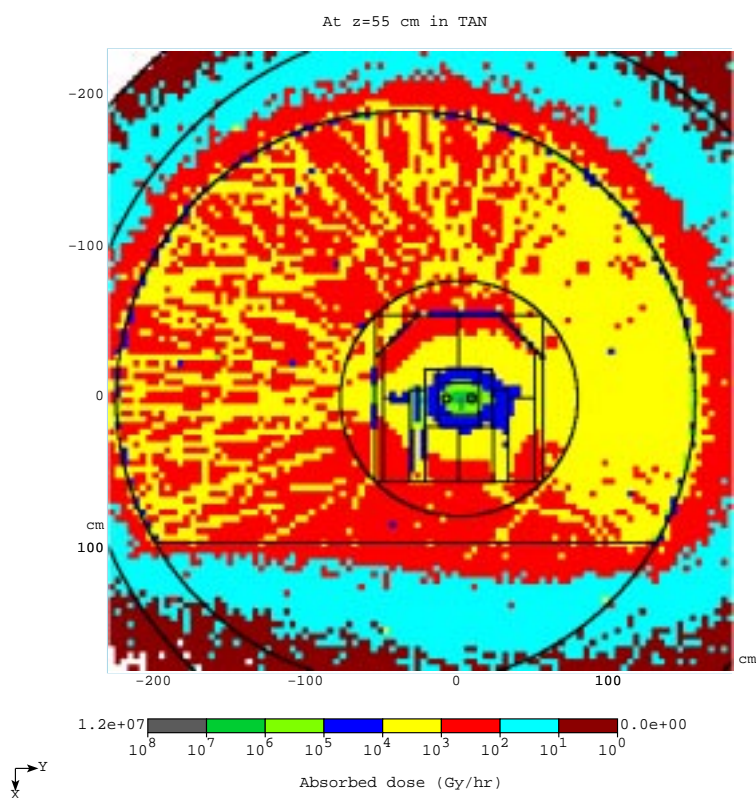
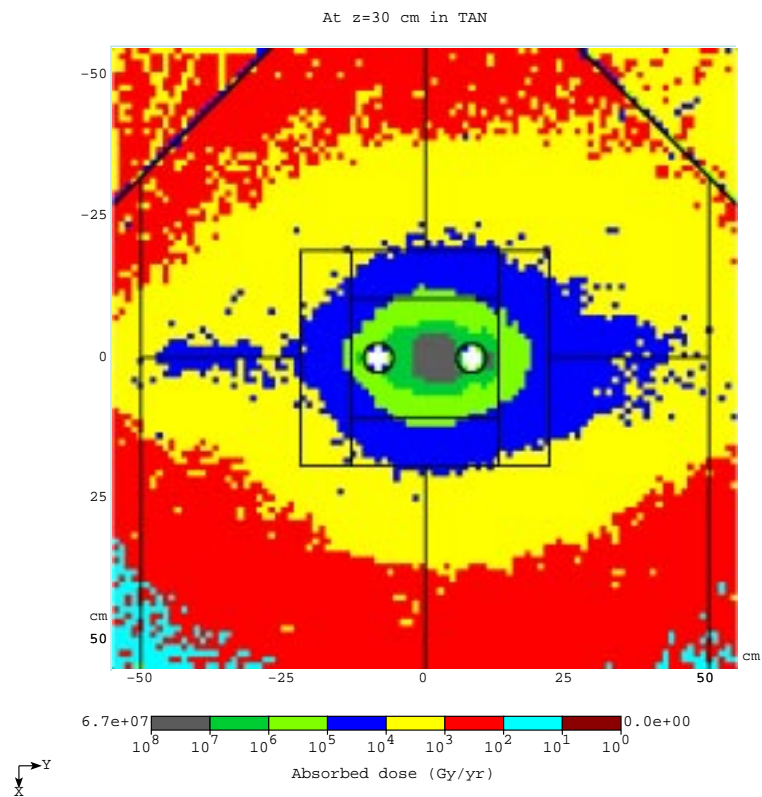


Figure 37: Yearly absorbed dose (Gy/yr) isocontours in the TAN and around at 30 cm (top) and 55 cm (bottom) from the entrance to the TAN core.

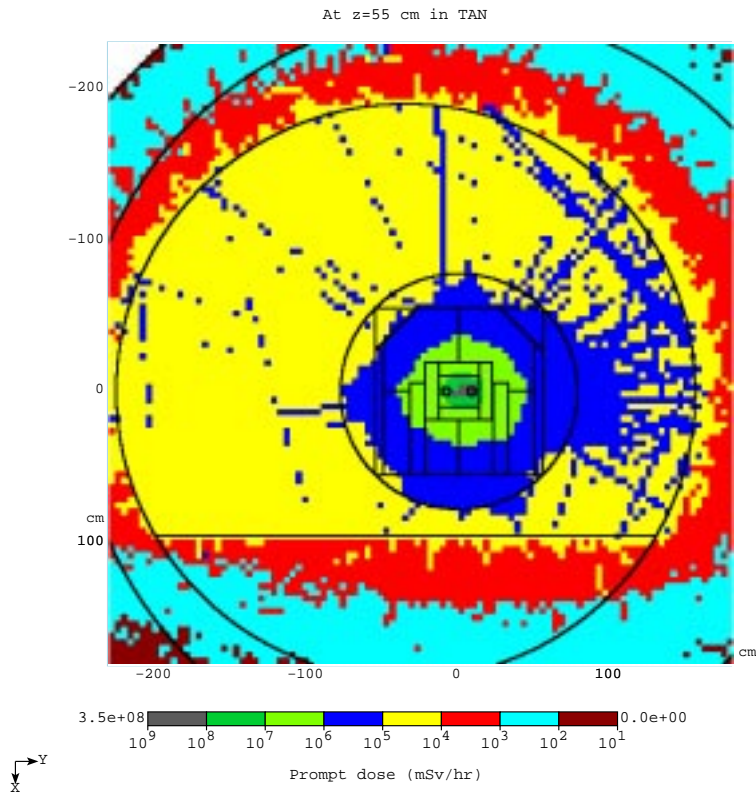
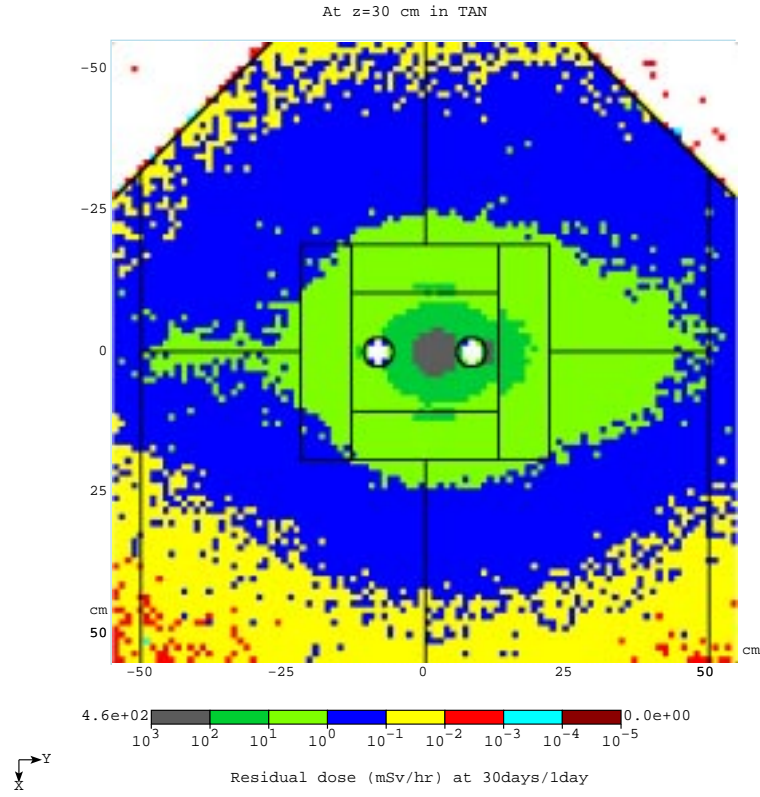


Figure 38: Residual 30day/1day dose on contact ($z=30$ cm, top) and prompt dose equivalent ($z=55$ cm, bottom) both in mSv/hr in the TAN and around.

Figs. 39 and 40 show azimuthally averaged isocontours of particle fluxes and dose values in the TAN-D2 region. One can see how nicely the TAN reduces radiation levels downstream, in the possible TOTEM location ($z=146.86\text{--}147.14$ m) and in the D2 separation dipole. Note that $x=y=R=0$ in these plots corresponds to the TAN core axis.

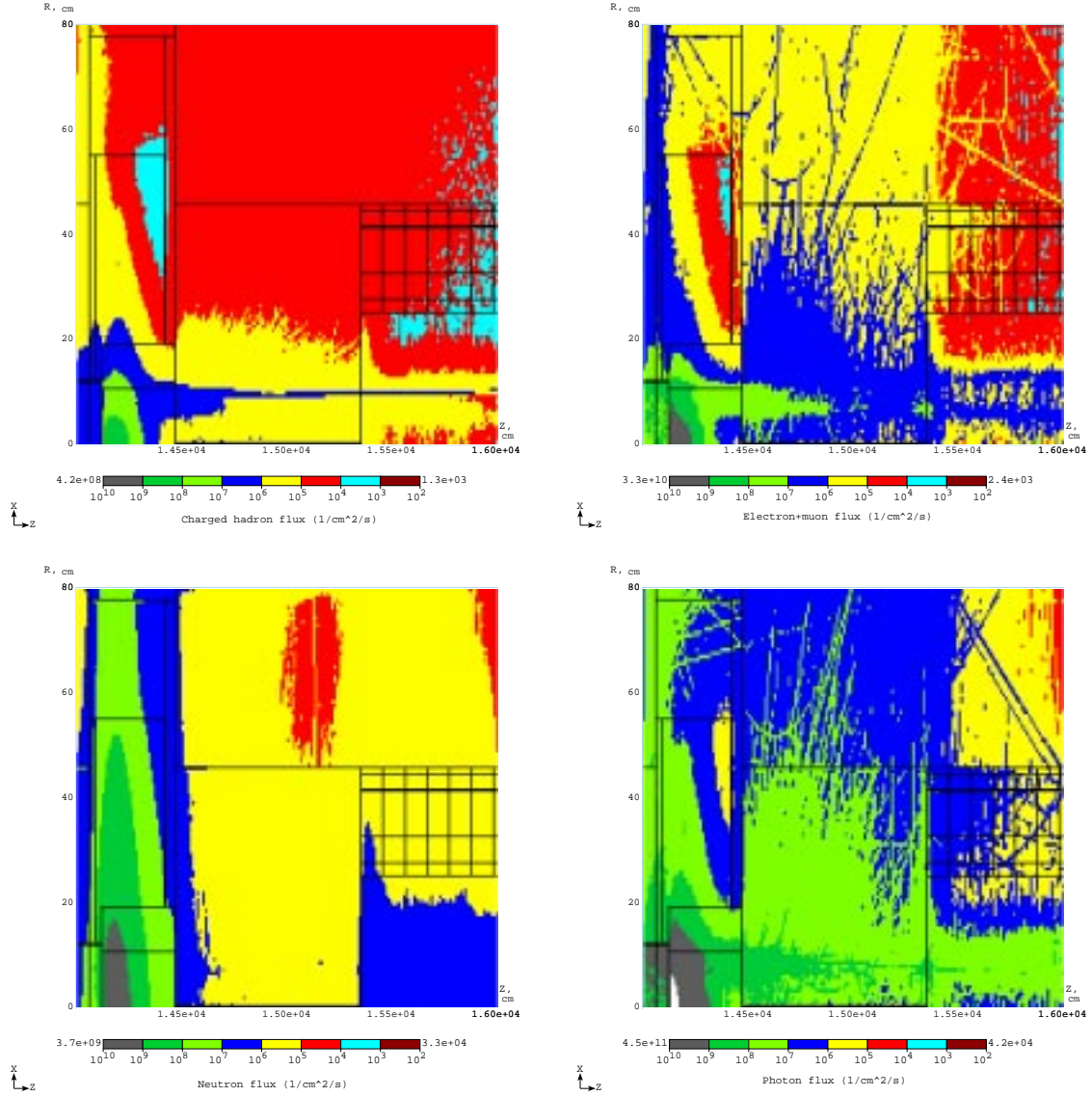


Figure 39: Azimuthally averaged charged hadron (left-top), neutron (left-bottom), electron+muon (right-top) and photon (right-bottom) flux isocontours ($E > 0.1$ MeV) in the IP5 TAN-D2 region: TAN at $z=140.6\text{--}144.7$ m, TOTEM at $z=146.86\text{--}147.14$ m, and D2 at $z=153.5\text{--}162.95$ m.

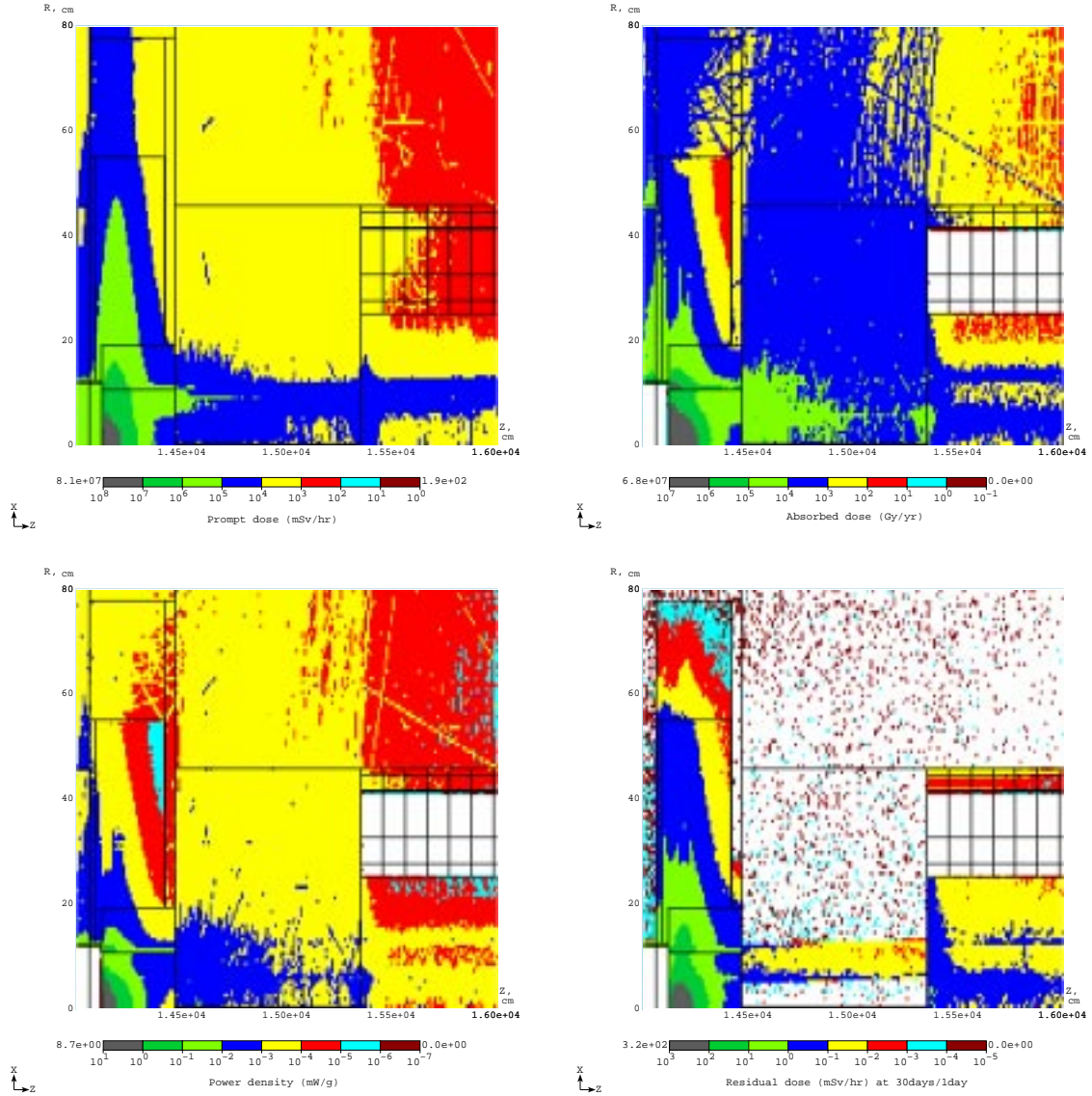


Figure 40: Azimuthally averaged prompt dose equivalent (left-top), power density (left-bottom), yearly absorbed dose (right-top) and 30day/1day residual dose (right-bottom) isocontours in the IP5 TAN-D2 region: TAN at $z=140.6\text{--}144.7$ m, TOTEM at $z=146.86\text{--}147.14$ m, and D2 at $z=153.5\text{--}162.95$ m.

The TOTEM Roman pots stations will be used for diffractive elastic scattering studies [23]. It implies severe restrictions on their design and positions because of high radiation load involved. The warm sections from D1 up to Q6 at IP5 are of interest, especially the region between TAN and D2 (see Fig. 29). To estimate possible radiation damage to the Roman pot electronics, calculations of particle fluxes around the beam pipe have been performed at the position of the second station ($z=146.86\text{--}147.14$ m). The results are given in Table 6. Corresponding energy spectra are presented in Fig. 41.

Table 6: Azimuthally averaged particle fluxes (in units of $10^5 \text{ cm}^{-2}\text{s}^{-1}$) at the second Roman pots station (150 m downstream of the IP5) *vs* distance from aperture axis at nominal luminosity. Energy cutoff is 0.1 MeV for all the particles. Estimated uncertainty in the given values is about 50%.

Particles	R (cm)					
	0.3	1	2	5	10	20
Neutrons	3.5	3.0	2.5	4.0	3.5	2.5
Charged hadrons	5.0	5.0	4.5	4.5	8.0	1.0
Photons	500	600	600	700	700	150
Electrons and positrons	30	50	50	60	60	10
Muons	0.1	0.1	0.1	0.08	0.07	0.05

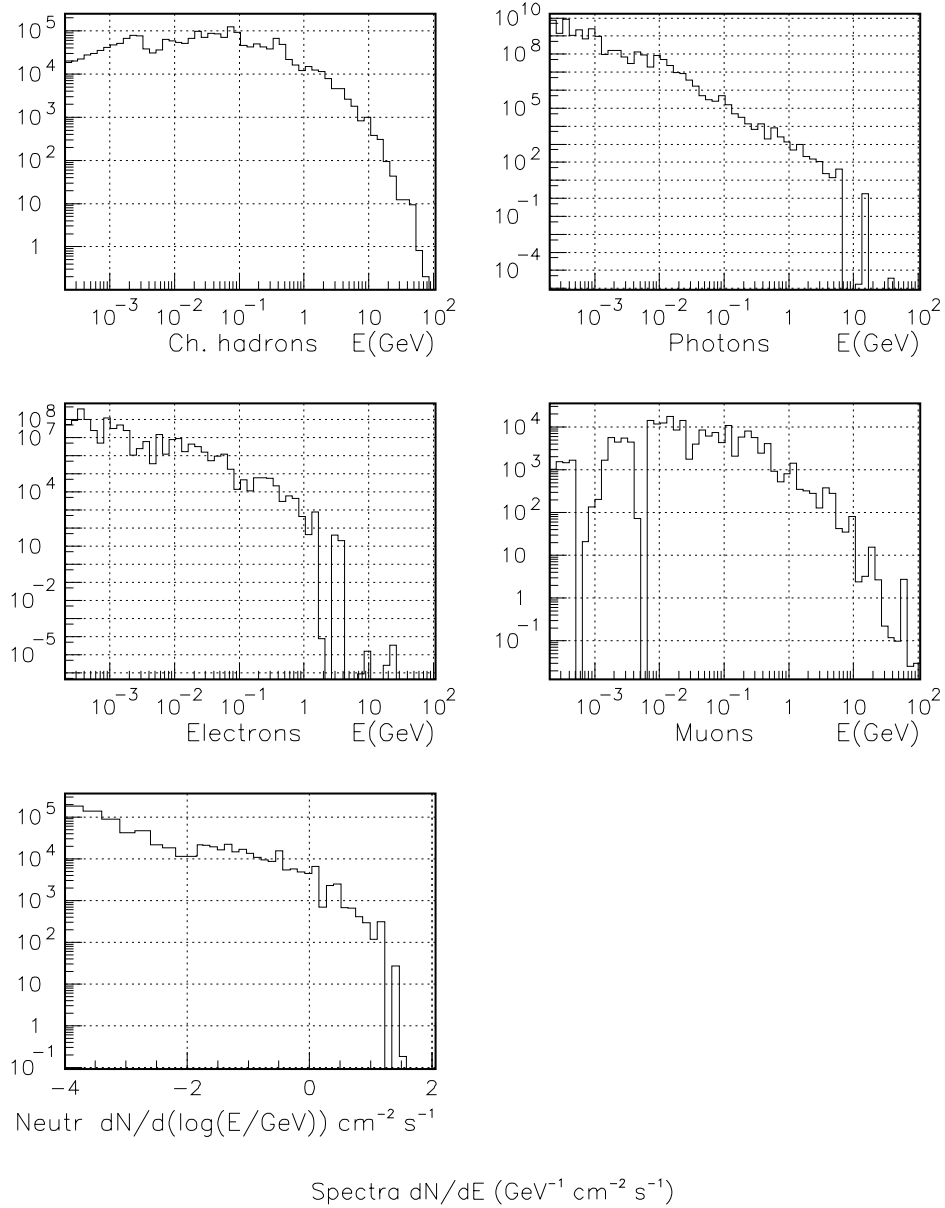


Figure 41: Particle spectra at the TOTEM station in the IP5 TAN-D2 region, averaged over $13 < r < 46$ cm.

5.3 Separation dipole and outer triplet

Radiation levels in the tunnel are given in Fig. 42 at 35 cm from the IP end of the D2 dipole.

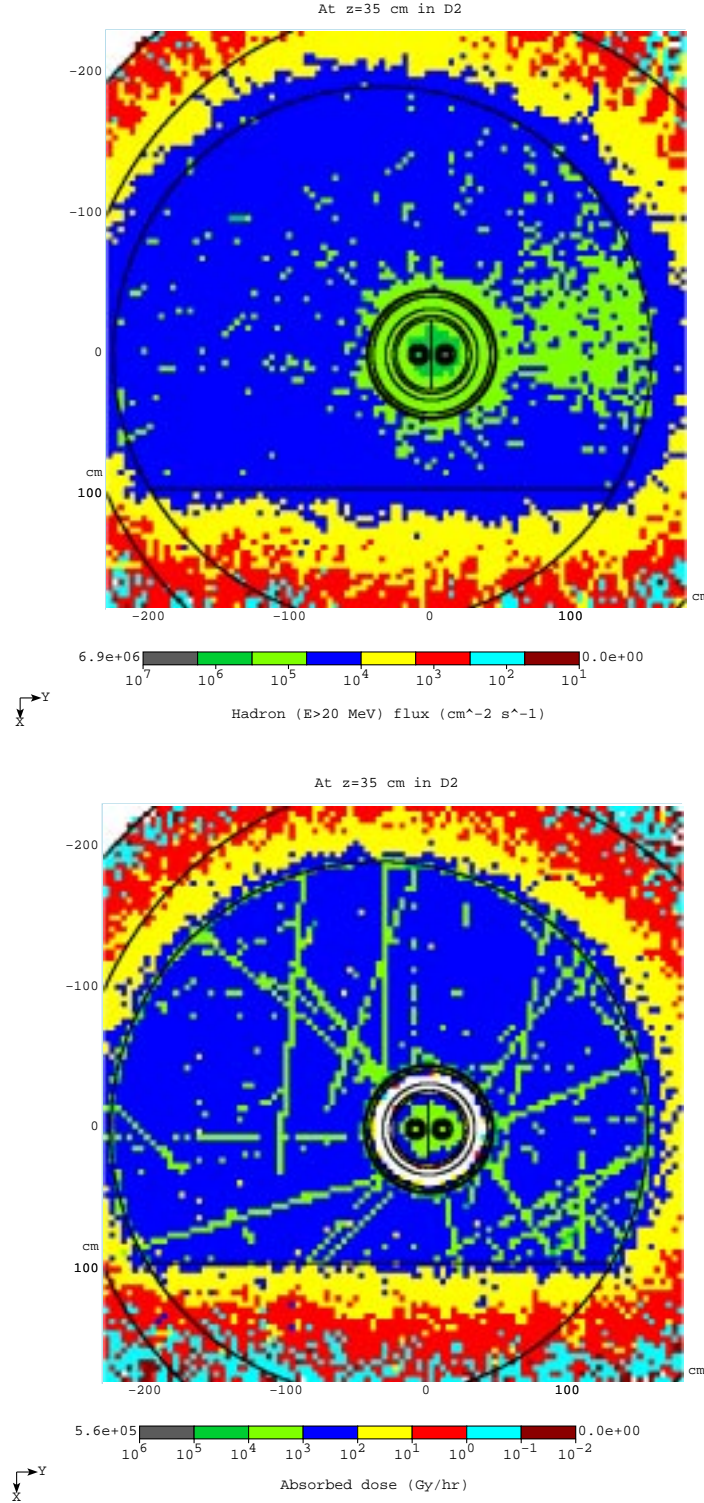


Figure 42: Hadron ($E > 20$ MeV) flux ($\text{cm}^{-2} \text{s}^{-1}$) (top) and yearly absorbed dose (Gy/yr) (bottom) isocontours in the tunnel cross-section at 35 cm from the IP end of the D2 dipole.

The TAN protects nicely the D2 dipole and Q4 quadrupole (Fig. 43), with the peak ϵ_{max} in the SC coils—which occurs again in a tiny azimuthal bin in the horizontal plane of the inner coil—almost a factor of a hundred below the tolerable limit, with about 1.85 W and 0.4 W of power dissipated in D2 and Q4, respectively. At the same time, calculations have shown that the peak power density in the Q5 SC coils was rather close to the allowable limit of 1.6 mW/g. It was found that an additional steel collimator TCL (former C45) $19.4 \times 19.4 \times 100$ cm³, situated between Q4 and Q5 after the BSRT at 190.9 m from the IP and with a 21.3 mm aperture for the outgoing beam (see Fig. 29), solves this problem. Fig. 44 shows that both the peak power density in the SC coils and power dissipation in the Q5 quadrupole calculated with such a collimator are similar to those in D2 and Q4. The price for that are rather high radiation levels around this collimator (Fig. 45).

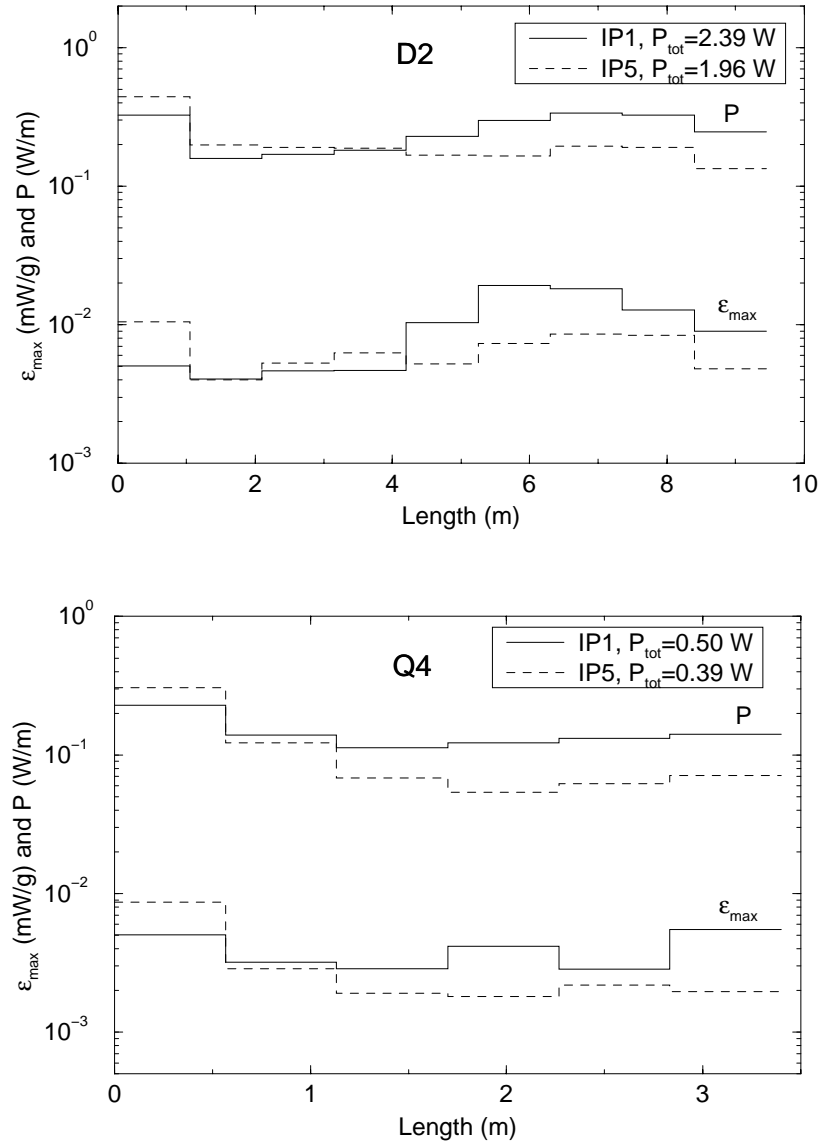


Figure 43: Peak power density ϵ_{max} and dynamic heat load P vs length in the IP1 and IP5 D2 separation magnet (top) and Q4 outer triplet quadrupole (bottom).

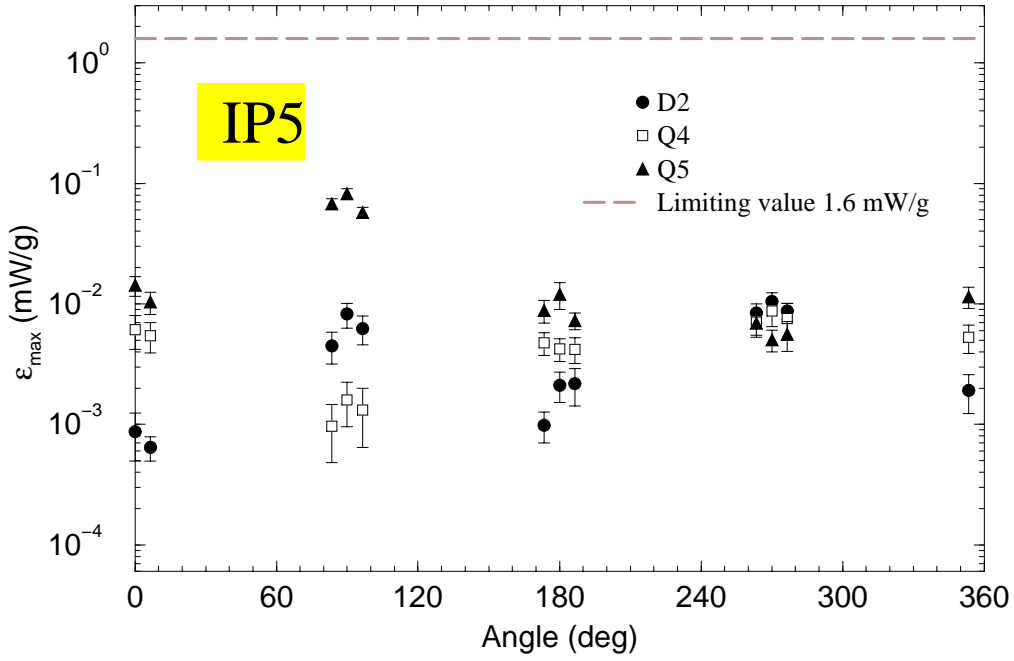
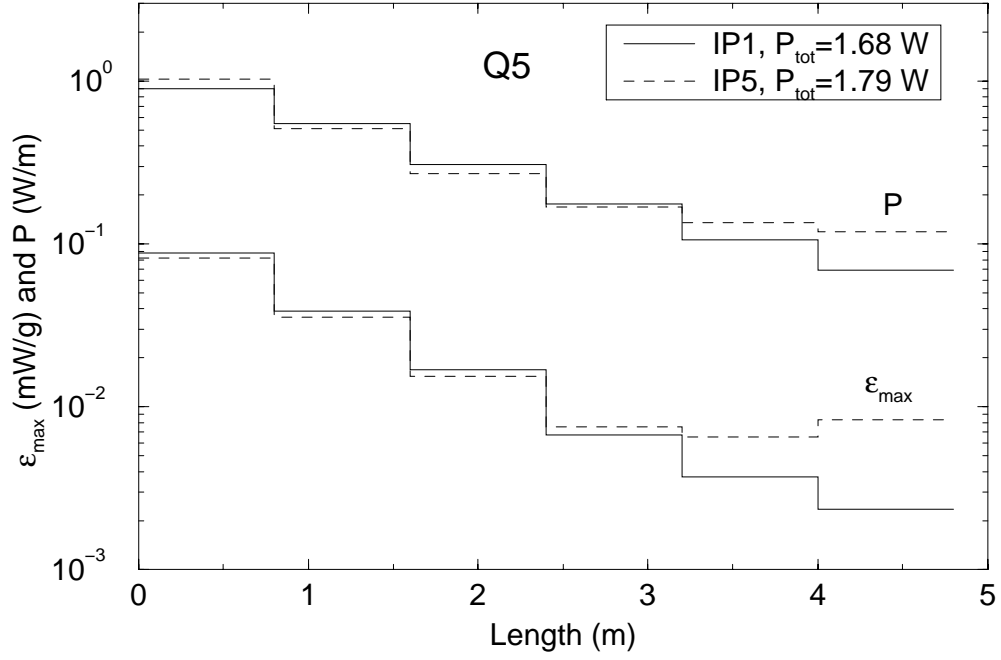


Figure 44: Peak power density ϵ_{\max} and dynamic heat load P vs length in the IP1 and IP5 Q5 outer triplet quadrupole (top) and distribution of peak power density ϵ_{\max} vs azimuth angle in the first layer in depth for the magnets considered (bottom).

Data on power dissipation for different components of the region are presented in Table 7. One can see that distributions of energy losses over components inside each of the longitudinal sections, calculated for IP1 and IP5, are similar. This result agrees with approximate symmetry in azimuth within the vessel incorporated in the model used. Total power dissipation, prompt dose and hadron fluxes for the outer triplet components are presented in Table 8. These results give dynamic heat load, useful information for beam loss monitor, and an estimate of radiation environment in the tunnel near the cryostat.

Table 7: Power dissipation (%) in the IP5/IP1 outer triplet region at nominal luminosity. Statistical error is 2-3%.

Element	D2	Q4	Q5
Beam Screen	8.3 / 9.8	21.2 / 20.9	12.1 / 11.5
Cold Bore (StSt)	11.6 / 13.2	17.9 / 18.8	12.5 / 12.3
Coolant (He)	0.2 / 0.2	0.2 / 0.3	0.2 / 0.2
Coil	21.5 / 22.6	41.6 / 38.2	45.9 / 44.3
Collar (StSt)	21.7 / 22.0	9.2 / 11.1	13.9 / 15.5
Yoke	30.6 / 27.4	7.5 / 9.0	13.3 / 14.2
Superinsulation	1.4 / 1.2	0.4 / 0.3	0.5 / 0.5
Vessel	4.7 / 3.6	2.0 / 1.4	1.6 / 1.5
Total (%)	100 / 100	100 / 100	100 / 100
Total (W)	1.96 / 2.39	0.39 / 0.50	1.79 / 1.68

Table 8: Dynamic heat load P (W) on the IP5 outer triplet components, and prompt dose equivalent DE (Sv/hr) and hadron flux Φ ($10^4 \text{cm}^{-2} \text{s}^{-1}$ at $E > 14$ MeV) on the vessel at longitudinal peaks at the nominal luminosity.

Element	P	DE	Φ
Absorber TAN	189		
Dipole D2	1.96	2.079	11.08
Quadrupole Q4	0.39	0.243	1.696
Quadrupole Q5	1.79	1.466	9.104

6 Uncertainties

Based on numerous international benchmarkings on micro and macro levels, status of the current event generators, thorough sensitivity analysis in the inner triplet over last eight years (event generators, physics other than event generators, geometry, materials, fields, crossing etc), numerous discussions and analyses of the results by the community over the same eight years, understanding of the Monte Carlo aspects, we would claim that we predict the maximum power density in the coils with an accuracy better than 30%. This should be true for the innermost layers of the SC coils (just a beginning of showers with almost no attenuation) for the *given* configuration, not for the one with possible changes. The uncertainty is higher at larger radii and larger distances from the IP, often because of statistics. Integral energy deposition and integral flux values in the components such as azimuthal average, power dissipation (dynamic heat load) are predicted with about 10-15% accuracy. Residual dose rates are estimated within a factor of two to three.

7 Summary

A protection system on each side of the IP1 and IP5 has been designed over the years on the basis of comprehensive MARS calculations. It includes:

- The TAS front copper absorber at L=19.45 m (1.8 m long, 34-mm ID, 500-mm OD).
- A 10-mm thick stainless steel (SS) liner in Q1.
- The SS absorber TASB at L=45.05 m (1.2-m long, r=33.3-60 mm). Proposed in earlier studies a TASA absorber at L=30.45 m (1.1-m long, r=25-60 mm) is eliminated from the design.
- A 3-mm thick beam pipe in the Q2A through Q3 region.
- The 40-cm long SS masks at L=23.45 m, r=250-325 mm to protect the Q1 slide bearings.
- The neutral particle copper absorber TAN at 140 m.
- The 1-m long TCL SS collimator at 191 m from the IP.

The system described in this paper and developed under realistic engineering constraints will protect the LHC IP1/IP5 region components against luminosity-driven short- and long-term deleterious energy deposition effects with a good safety margin, at least at the design luminosity of $10^{34} \text{ cm}^{-2} \text{ s}^{-1}$.

8 Acknowledgments

We express our gratitude to M. Karppinen, V.V. Kashikhin, M. Lamm, T. Ogitsu, R. Ostojic and G. Sabbi for magnetic field maps calculated with POISSON and OPERA for KEK and FNAL low- β quadrupoles, separation dipoles D1 and D2, and quadrupoles of the outer triplet and to J. Zbasnik for description of the DFBX feedbox.

References

- [1] The Large Hadron Collider Conceptual Design, CERN/AC/95-05(LHC), 1995, P. Lefèvre and T. Pettersson, editors.
- [2] N.V. Mokhov, “Accelerator-Experiment Interface at Hadron Colliders: Energy Deposition in the IR Components and Machine Related Background to Detectors”, Fermilab-Pub-94/085 (1994).
- [3] A. Morsch, R. Ostojic, T.M. Taylor, “Progress in the Systems Design of the Inner Triplet of 70 mm Aperture Quadrupoles for the LHC Low-beta Insertions”, Proc. 4th European Part. Accel. Conf., London, England, 1994.
- [4] N.V. Mokhov, J.B. Strait, “Optimization of the LHC Interaction Region with Respect to Beam-Induced Energy Deposition”, EPAC96 and Fermilab-Conf-96/136 (1996).
- [5] N.V. Mokhov, J.B. Strait, Proc. of the 1997 Part. Accel. Conf., Vancouver, B.C., Canada, May 1997, p. 124.
- [6] N.V. Mokhov, I.L. Rakhno, “Protecting LHC Components Against Radiation Resulting from Colliding Beam Interactions”, Proc. of the 2001 Part. Accel. Conf., Chicago, June 2001, p. 3165; Fermilab-Conf-01/131 (2001).
- [7] L. Burnod, et al., “Thermal Modelling of the LHC Dipoles Functioning in Superfluid Helium”, Proc. 4th European Part. Accel. Conf., London, England, 1994.
- [8] R. Bossert, et al., “Development of a High Gradient Quadrupole for the LHC Interaction Regions”, IEEE Trans. Appl. Superconductivity **7**, 1997.
- [9] A.V. Zlobin, E. Barzi, D. Chichili *et al.*, “Large-Aperture Nb₃Sn Quadrupoles for 2nd Generation LHC IRs”, Proc. of the European Particle Accelerator Conference, Paris, June 3-7, 2002, pp. 2451-2453; <http://accelconf.web.cern.ch/accelconf/e02/PAPERS/MOPLE017.pdf>.
- [10] N.V. Mokhov, “The MARS Code System User’s Guide”, Fermilab-FN-628 (1995); N. V. Mokhov, O. E. Krivosheev, “MARS Code Status”, Proc. of the Monte Carlo 2000 Conference, Lisbon, October 23-26, 2000, Springer, p. 943; Fermilab-Conf-00/181 (2000); <http://www-ap.fnal.gov/MARS/>
- [11] S. Roesler, R. Engel, J. Ranft, Proc. of the Monte Carlo 2000 Conference, Lisbon, October 23-26, 2000, Springer, p. 1033.
- [12] <http://proj-lhc-optics-web.web.cern.ch/proj-lhc-optics-web/V6.2/OpticsSource.link/V6.2.seq>, <http://proj-lhc-optics-web.web.cern.ch/proj-lhc-optics-web/V6.4/>.
- [13] J.B. Jeanneret and T. Risselada, “Geometrical Aperture in LHC at Injection”, LHC Project Note 66 (1996).
- [14] O. Bruning, W. Herr, R. Ostojic, “A Beam Separation and Collision Scheme for IP1 and IP5 at the LHC for Optics Version 6.1”, LHC Project Report 315 (1999).
- [15] A.I. Drozhdin, M. Huhtinen, N.V. Mokhov, Nucl. Instr. and Methods, **A381**, 531 (1996).
- [16] A.I. Drozhdin, N.V. Mokhov, M. Huhtinen, Proc. of the 1999 Part. Accel. Conf., New York, 1999, p. 1231.

- [17] N.V. Mokhov, A.I. Drozhdin, I.L. Rakhno, M. Gyr, E. Weisse, “Protecting LHC Components Against Radiation Resulting from an Unsynchronized Beam Abort”, Proc. of the 2001 Part. Accel. Conf., Chicago, June 2001, p. 3168; Fermilab-Conf-01/133 (2001).
- [18] K. Potter, G.R. Stevenson, “Average Interaction Rates for Shielding Specification in High-Luminosity LHC Experiments”, LHC Note 310 (1995); CERN LHC-PM-ES-0002.00; M. Huhtinen and G.R. Stevenson, private communication; N.V. Mokhov, Memo of February 12, 1999.
- [19] N.V. Mokhov, “Reduction of Radiation Dose in Q1 Slide Bearings”, Fermilab Memo of October 2, 2001.
- [20] T. Sen, J. Strait, A. V. Zlobin, “Second generation high gradient quadrupoles for the LHC interaction regions”, Proc. of the 2001 Part. Accel. Conf., Chicago, June 2001, p. 3421.
- [21] E. Gschwendtner, M. Placidi, H. Schmickler, “Polycrystalline CdTe Detectors: A Luminosity Monitor for the LHC”, presented at 8th Topical Seminar on Innovative Particle and Radiation Detectors, October 2002, Siena, Italy.
- [22] E.H.Hoyer, W.C. Turner, N.V. Mokhov, Proc. of the 6th European Part. Accel. Conf., Stockholm, 1998, p. 368.
- [23] G. Matthiae, “Programme and status of TOTEM”, Proc. of the Int. Conf. on Elastic and Diffractive Scattering, Průhonice near Prague, Czech Republic, June 9-15, 2001, p. 355; S. Grohmann, V. Eremin, W. Kienzle *et al.*, “Detector development for TOTEM Roman pots”, *Ibid.*, p. 363.